UNIVERSITY OF CALIFORNIA
RIVERSIDE

Combined Optical Micro Manipulation, Force Microscopy, and Quantitative Phase Imaging for Studying Cellular Membrane Protrusion Dynamics

A Dissertation submitted in partial satisfaction
of the requirements for the degree of

Doctor of Philosophy

in

Bioengineering

by

Mohammad Sarshar

March 2016

Dissertation Committee:
Dr. Bahman Anvari, Chairperson
Dr. Hyle Park
Dr. William Grover

The Dissertation of Mohammad Sarshar is approved:

Committee Chairperson

University of California, Riverside

ABSTRACT OF THE DISSERTATION

Combined Optical Micro Manipulation, Force Microscopy, and Quantitative Phase Imaging for Studying Cellular Membrane Protrusion Dynamics

by

Mohammad Sarshar

Doctor of Philosophy, Graduate Program in Bioengineering
University of California, Riverside, March 2016
Dr. Bahman Anvari, Chairperson

Optical tweezers have become an important instrument in force measurements associated with various physical, biological, and biophysical phenomena. Quantitative use of optical tweezers relies on accurate calibration of the stiffness of the optical trap. In the first chapter, a comparative study of methods in calibrating the stiffness of a single beam gradient force optical trap at trapping laser powers is provided. The Equipartition theorem and Boltzmann statistic methods demonstrate a linear stiffness with trapping laser powers up to 355 mW, when used in conjunction with video position sensing means. The Power Spectral Density (PSD) of a trapped particle's Brownian motion, or measurements of the particle displacement against known viscous drag forces, can be reliably used for stiffness calibration of an optical trap over a greater range of trapping laser powers. Viscous drag stiffness calibration method produces results relevant to applications where trapped particle undergoes large displacements, and at a given

position sensing resolution, can be used for stiffness calibration at higher trapping laser powers than the PSD method. The efficacy of optical tweezers is limited in applications where concurrent metrology of the nano-sized structure under interrogation is essential to the quantitative analysis of its mechanical properties and various mechanotransduction events. In the second chapter I report on developing a platform for combined optical micromanipulation and interferometric topography (COMMIT). The all-optical platform delivers pN force resolution in parallel to ≈ 30 nm (or better) axial resolution in biological samples. Plasma membrane tethers are involved in various cellular functions such as motility, cell communications, and transmission of pathogens. In the third chapter, I report on using the COMMIT platform for simultaneous extrusion, force microscopy, and super resolution imaging of membrane tethers from cytoskeleton intact and disrupted HEK239 cells. COMMIT enabled label-free observation of the force-active sub-resolution heterogeneities in tether diameter along its length. I report on observation of cell's active maintenance of low membrane curvature at the base of the tether to facilitate tether tension relaxation by the Marangoni flow. I also show that the cell is capable of inducing functional shape changes in the tether even in the absence of a functional cytoskeleton.

Acknowledgments

Creation of the chapters of this thesis has been made possible with the support of my co-authors of the studies presented in each chapter:

Chapter 1: Winson Wong and Dr. Bahman Anvari.

Chapter 2: Thompson Lu and Dr. Bahman Anvari.

Chapter 3: Thompson Lu, Andrew Nguyen, and Dr. Bahman Anvari.

The first chapter of this thesis was published in the Journal of Biomedical Optics (doi: 10.1117/1.JBO.19.11.115001). This work was supported in part by a grant from the National Institutes of Health (2R01-DC02775) and National Science Foundation (BES-0522862). Additional support was provided by Bourns College of Engineering and the Center for Bioengineering Research at the University of California, Riverside.

For my beloved mother, ***Parvin****,*

and the loving memory of my father, ***Abolhassan****.*

Table of Contents

List of Figures

Chapter 1

Chapter 2

Chapter 3

Appendix

Chapter 1

A comparative study of methods to calibrate the stiffness of a single beam gradient force optical tweezers over various laser trapping powers

Abstract. Optical tweezers have become an important instrument in force measurements associated with various physical, biological, and biophysical phenomena. Quantitative use of optical tweezers relies on accurate calibration of the stiffness of the optical trap. Using the same optical tweezers platform operating at 1064 nm and beads with two different diameters, we present a comparative study of viscous drag force, Equipartition theorem, Boltzmann statistics, and Power Spectral Density (PSD) as methods in calibrating the stiffness of a single beam gradient force optical trap at trapping laser powers in the range of 0.05-1.38 W at the focal plane. The Equipartition theorem and Boltzmann statistic methods demonstrate a linear stiffness with trapping laser powers up to 355 mW, when used in conjunction with video position sensing means. The PSD of a trapped particle's Brownian motion, or measurements of the particle displacement against known viscous drag forces can be reliably used for stiffness calibration of an optical trap over a greater range of trapping laser powers. Viscous drag stiffness calibration method produces results relevant to applications where trapped particle undergoes large displacements, and at a given position sensing resolution, can be used for stiffness calibration at higher trapping laser powers than the PSD method.

Keywords: Boltzmann statistics; Equipartition theorem; power spectral density; viscous drag; CCD camera; quadrant photodetector.

1.1 Introduction

Since its introduction by Ashkin,[1] optical tweezers have been used in a broad range of application in biology,[2-16] physics,[17-23] and biophysics.[24-31] The pico-Newton force resolution offered by optical tweezers, and its non-invasive nature render it as a useful instrument in cell manipulation,[32-35] and force microscopy studies.[21] Use of optical tweezers in quantitative studies requires accurate calibration of the optical trap stiffness. Considerable efforts have been made in developing calibration techniques, or improving their efficiency and accuracy.[36-53] In general, stiffness calibration methods for optical tweezers are divided into three categories. In the first category (also referred to as *active* stiffness calibration methods), optical trap stiffness is obtained by calibration of the laser-mediated optical force against a known externally applied force. An example of an applied external force is the Stokes' drag experienced by an optically trapped particle in response to relative movement between the trapped particle and the fluid in which the particle is trapped. Under this approach, either the trapping chamber is moved against a fixed optical trap, or calibrated movements are applied to a steerable trapped particle within the trapping chamber.[5-10, 53-57]

In the second (*passive*) stiffness calibration category, several calibration methods exist to estimate the stiffness of the optical tweezers by analyzing the thermal fluctuations of the trapped particle.[58] Position variance of a trapped particle is used to calculate the optical tweezers stiffness by modeling the behavior of the particle using Equipartition theorem. In another approach, the optical trap's potential is reconstructed using Boltzmann statistics.[58] Using this method, the stiffness is measured using the complete

distribution of the trapped particle's positions within the optical trap.[59, 60] Alternatively, using the Power Spectral Density (PSD) method, a trapped particle's thermal noise is analyzed in the frequency domain to determine the optical trap's stiffness.[41]

The third (*direct*) category estimates the optical trap's stiffness by measuring the changes in momentum of scattered trapping light.[39, 61, 62] This approach usually requires a dual beam trap and collection of the entire scattered light. The direct calibration method has recently been applied to single beam traps[50, 63] in conjugation with back focal plane interferometry, but is not yet commonly employed.

The absolute optical trap stiffness measured at a given trapping laser power depends on the calibration approach employed. Variations in reported trap stiffness have been attributed to uncertainties associated with the method used to calibrate the trap stiffness, and can lead to discrepancies in reported forces associated with common biological phenomena.[64] Although comprehensive theoretical and experimental studies of each stiffness calibration approach are reported in the literature, a side-by-side study of such approaches in measuring an optical trap's stiffness over a range of trapping laser powers will help evaluate the efficacy of each calibration technique in practice, and better understand the discrepancies among the stiffness values they report.

Detecting the displacements of a particle within the optical trap is a crucial part in all aforementioned calibration methods. Both low bandwidth (<1 kHz) and high bandwidth (usually in the range of 10-70 kHz) position sensing means are used to track the displacements of an optically trapped particle. We used a CCD camera as low bandwidth, and a quadrant photodetector (QPD) as high bandwidth position detection means to

assess the ability of low bandwidth and high bandwidth particle tracking schemes in calibrating optical trap stiffness over trapping laser powers in the range of ≈ 0.05-1.38 W. The QPD can be aligned either in a basic manner to track the image (or the shadow) of a trapped particle much like in video particle tracking, or in an enhanced manner, to track the trapped particle using the forward scattered laser off the particle. In the later configuration, the interference pattern resulting from unscattered trapping laser (or a second low-power tracking laser) and the forward scattered laser from the bead is projected onto the QPD at the back focal plane of the condenser lens.

The back focal plane interferometry configuration improves the spatial resolution beyond what the imaging configuration offers, but requires using a high numerical aperture (N.A.) condenser lens matching the N.A. of the trapping microscope objective in order to collect the entire scattered laser light. While the QPD can be used in imaging mode for particle tracking in virtually any optical trapping setup, the use of forward scattered light is limited due to its necessary design considerations and optics. As an example, when optical tweezers are combined with other modes of biophysical experimental techniques such as patch clamp,[65] a high N.A. condenser can no longer be used to collect the scattered laser light for particle trapping.

In this study, we utilized an optical tweezers setup with design considerations applicable to most common biophysical investigations, and used different calibration methods to compare the transverse stiffness of the trap over various trapping laser powers. Specifically, we first obtained the optical trap stiffness by applying known viscous drag forces against an optically trapped polystyrene bead at various laser output

powers (i.e., active stiffness calibration method). To compare with the passive stiffness calibration methods, we performed a series of calibration experiments based on the PSD, Equipartition theorem, and Boltzmann statistics methods over the same range of trapping laser powers.

Stiffness of an optical trap changes with the size of the optically trapped particle. The maximum optical trapping forces experienced by beads (micro- or nano- sized spheres) have a non-linear correlation with the bead radius (r). For a trapping laser wavelength of λ=1064 nm, maximum optical forces experienced by small volume (r < 100 nm) trapped beads have been shown to increase to the third power of the radius (r^3) in the Rayleigh regime,[36, 66] with the exponent decreasing beyond the 100 nm range.[67] For beads with large volumes (r> 10 μm), the maximum optical force experienced by the particle decreases with an inverse relation to its radius.[68]

Significant attempts have been made to model the trapping optical forces experienced by a particle in different volume scales. Earlier models[69] suggested that the size dependency of the maximum trapping forces experienced by beads can be described using the electromagnetic theory in the small-volume scale, and ray optics in the large-volume scale. The mid-volume scale particles that are most commonly used in biophysical studies were first successfully included in a multi-scale electromagnetic model by Rohrbach,[70] who studied the optical trap stiffness as a function of the bead radius in the range of 0.11 μm to 0.5 μm. Neto and Nussenzveig used the Mie theory to model the axial[71] and transverse[72] optical trapping forces on beads, which can also be expanded to predict the optical forces on particles in the ray optics regime. Accuracy of

such multi-scale models are improved by further optical characterizations of the tweezers setup such as accounting for spherical aberrations[73] and astigmatism.[74]

In addition to the radius-dependent differences in how particles in different volume-scales interact with the highly focused laser in optical traps, other particle characteristics such as the refractive index[68] and polarizability[75] affect the optical trap stiffness as well. Moreover, it has been recently shown that the dynamic behavior of optically trapped micro particles in viscous media transitions from an over-damped regime for larger particles ($r > 1$ μm) to an under-damped regime for smaller particles ($r < 250$ nm).[76]

Herein, we have used particles of two different sizes within the Mie regime, and compared the results of different calibration methods on particle size dependence of the optical trap stiffness. Under the high bandwidth position sensing scheme, we calibrated the optical trap stiffness using the PSD and viscous drag force methods. We used the Equipartition theorem and Boltzmann statistic calibration methods to calibrate the optical trap stiffness under the low bandwidth position detection scheme. We demonstrate that employing different calibration methods and position sensing means report different stiffness values for an optical trap, and discuss practical advantages and disadvantages of each approach.

1.2 Methods

1.2.1 Experiment setup

1.2.1.1 Optical trap formation

Schematic of the experimental setup is shown in Fig. 1.1. The optical trap was formed on an inverted microscope (Ti-Eclipse, Nikon Inc., Melville, NY) using a 100X oil

immersion objective lens with 1.49 N.A. and 120 μm working distance (Apo TIRF, Nikon). A solid state Nd:YVO_4 laser (Prisma 1064-V, Coherent, Santa Clara, CA) generating a laser beam with a 1064 nm wavelength, and in TEM_{00} mode was used for optical trapping. The laser beam was expanded by a set of plano-convex lenses to slightly over-fill the back aperture of the microscope objective. The output power of the trapping beam was measured at the back aperture of the objective lens by a power meter (PD300, Ophir Optronics, North Andover, MA). We used beads with two different diameters for trapping. The smaller beads were sulfate-modified fluorescent polystyrene beads 4.2 ± 0.21 (mean ± standard deviation) μm in diameter (F-8858, Molecular probes, Eugene, OR). These beads had an excitation spectrum between 480 and 590 nm with peak fluorescence emission at 605 nm when photo-excited at 580 nm. We refer to these particles as "red" beads. In addition to the 4 μm diameter red beads, we used larger polystyrene beads, approximately twice in diameter (8 ± 0.7 μm) (2106E, Phosphorex, Hopkinton, MA) while maintaining a comparable position tracking signal to the noise ratio (SNR) between the experiments. These beads had an excitation spectrum between 400 and 490 nm with peak fluorescence emission at 500 nm when photo-excited at 460 nm. We refer to these particles as "green" beads. Both particles were chosen within the same volume-scale to limit the uncertainties related to the volume-dependent differences in how particles in different volume-scales interact with the highly focused laser in optical traps. Beads were suspended in deionized (DI) water during optical trapping experiments.

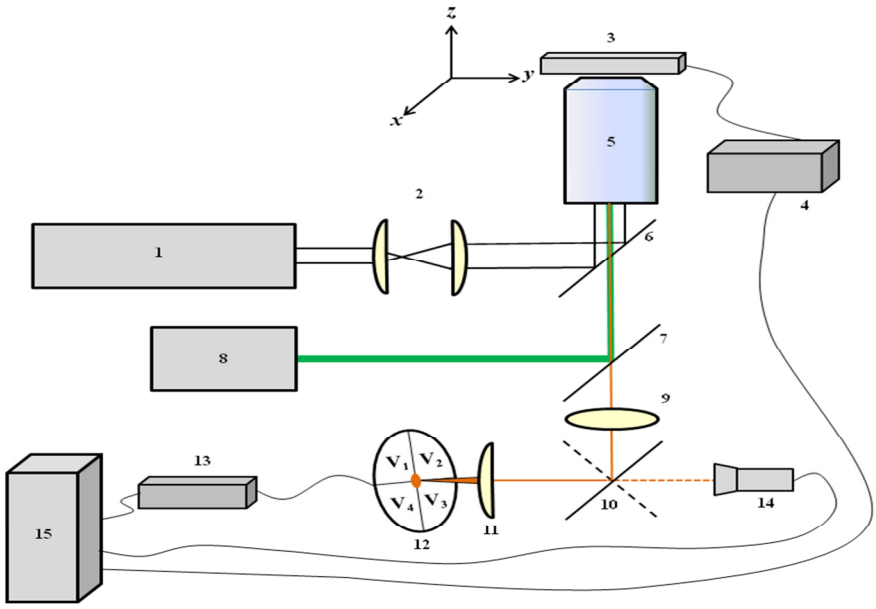

Fig. 1.1 Schematic of the experimental setup. 1. Nd:YVO_4 laser. 2. Beam expander. 3. PZT stage. 4. PZT controller. 5. 100X microscope objective. 6. Dichroic mirror. 7. TRITC/FITC filter set. 8. Arc lamp. 9. Condenser. 10. Steering mirror. 11. Focusing optics. 12. Quadrant photodetector (QPD). 13. Analog to digital converter. 14. CCD Camera. 15. Computer.

The trapping laser beam (1064 nm) can give rise to two-photon absorption phenomena in red fluorescent beads over all trapping laser powers. To investigate the effects of two-photon absorption on the measured stiffness, we repeated the trap stiffness calibrations using a control bead that had similar material properties and drag coefficient to those of the red fluorescent beads, but without significant two-photon absorption over the trapping laser powers. Specifically, we used 4.18±0.4 μm diameter dragon green fluorescent beads (Bangs Laboratories, Inc., Fishers, IN) with peak absorption and emission at 480 nm and 520 nm, respectively. We repeated the trap stiffness calibrations using the viscous drag force method over the low (51 and 136 mW), medium (674 mW), and high (1.38 W) laser powers (delivered at the specimen plane) in samples containing

both 4 μm beads, with results presented in section 3.2.1. We used a dichroic beam splitter with over 90% transmittance between 470 nm and 650 nm, and over 98% reflectance at 1064 nm (680dcspxr-laser, Chroma Technology Corp, Bellow Falls, VT) to stir the laser beam towards the objective. The optical setup allowed for simultaneous trapping and fluorescent imaging of the trapped beads.

The transmission of the microscope objective at 1050 nm and 1100 nm are reported by the manufacturer as 60% and 57%, respectively. We assumed a 60% transmission for the objective lens at 1064 nm which is in agreement with other reports[77-79] that measured the transmittance of high N.A. microscope objectives of the same brand and similar optical properties at 1064 nm using the dual objective method.[79-81] We increased the laser output power in eight steps from 85 mW to a maximum power of 2.294 W, measured at the back pupil of the objective. The calculated trapping laser powers delivered to the specimen plane ranged between 51 mW and 1.376 W.

We measured the temperature of the DI water using a thermistor connected to a Vernier LabQuest device (Vernier Software & Technology, Beaverton, OR). The mean ± standard deviation value of water temperature was 24.98±0.23 °C (water dynamic viscosity η=0.8925·10^{-3} Pa·s at T=24.98 °C). The laser-induced temperature increase, which occurs within the laser focus, has a significant effect on the measured trap stiffness through its effect on the viscosity of the medium and the thermal motion of the trapped particle.[78, 82] This effect becomes more pronounced at higher trapping laser powers, and higher trapping depths when using an oil immersion microscope objective.[83] We accounted for these effects by assuming a temperature increase of 8 K/W at 1064 nm in

DI water as our optical trapping medium.[78] Therefore, the expected range of the DI water temperature in our experiments during the applied range of trapping powers was ≈ 24.98-35.99 °C. Furthermore, all experiments were conducted within 30 seconds of the initial trapping of the bead to avoid or minimize excessive temperature build up at laser focus.

1.2.1.2 Fluorescence and bright field imaging and position detection

Both white light and fluorescence modes can be used for particle tracking using the QPD in the imaging configuration. Under white light, the contrast between the shadow of the optically trapped particle and the bright background is used for particle tracking. In fluorescence, the emission from a fluorescent probe against the dark background is used to track the optically trapped fluorescent particle. For bright field imaging of the particles, a 100W Tungsten lamp (TI-DH Diascopic Illumination Pillar, Nikon) was used to illuminate the samples. For fluorescence imaging of the particles, an arc lamp (LUDL Electronic products, Hawthorne, NY) was used to optically excite the fluorescent beads.

We used A TRITC-B-NTE filter set (Semrock, Rochester, NY) to optically excite the red fluorescent beads in the 530-550 nm band and collect the fluorescence emission in the 570-620 nm range. A FITC-3540B-NTE filter set (Semrock), which allows the transmission of an excitation band in the range of 446-500 nm, and an emission band of 513-725 nm, was used during the optical excitation of the green fluorescent beads and collection of fluorescence emission. For comparative purposes, we employed two commonly used position sensing methods: first, a non-video position detection using a Quadrant photodiode (QPD) (QP50-6SD, Pacific Silicon Sensor, Westlake Village, CA),

and second, video particle tracking using a CCD camera (C9100-13, Hamamatsu Corp., Bridgewater, NJ).

Using the QPD allowed for high bandwidth position recordings with sampling frequencies in the kHz range. The QPD was aligned such that the image position along the primary *x*, *y*, and *z* axes of the lab were respectively proportional to differential voltages $V_x = (V_1 + V_4) - (V_2 + V_3)$, $V_y = (V_3 + V_4) - (V_1 + V_2)$, and the sum voltage $V_S = V_1 + V_2 + V_3 + V_4$ (where V_{1-4} are diode voltages). Differential voltages were digitized by an analog-to-digital converter (BNC-2110 and NI PCI-6133, National Instrument, Austin, TX), and stored in a computer using LabVIEW software (version 8.2, National Instruments) for further analysis. Additionally, bead positions were determined using a CCD camera. For this purpose, images of the fluorescent bead were acquired at 179 frames per second (fps) by HCImage software (version 2,0, Hamamatsu), and analyzed in MATLAB™ (The MathWorks, Natick, MA) for particle tracking.

1.2.2 Displacement calibrations

1.2.2.1 QPD-based position sensing

To accurately control the position of the optical trapping chamber, and apply viscous drag forces of known magnitude on trapped particles, we used a piezoelectric translation-stage (PZT) (P-527.C3, Physik Instrumente, Waldbronn, Germany) with a transverse resolution of <10 nm. Output voltage of the QPD was calibrated against displacement using the PZT as follows. The position of a trapped bead in the field of view was initially taken as the reference point to center the QPD. Subsequently, in the absence of the optical trap, a bead

was attached to the cover slip and brought to the exact transverse position of the trapped bead using the PZT. The fluorescent image of the bead (or the shadow of the bead when white light was used for particle tracking) was centered on the QPD by moving the QPD using a 3D translational stage.

Next, the bead was displaced multiple times in steps of known increments (0.01-1 μm) using the PZT while QPD's differential voltages were recorded. Recording of larger bead displacements (up to 1 μm) in *x* and *y* directions showed that the QPD response within this range was linear. Finally, a linear fit to the displacement-voltage data points provided a voltage-displacement calibration equation for the QPD. The differential voltages V_x and V_y were normalized by V_S to create normalized output-displacement calibration graphs in *x* and *y* directions. The slope of the linear fit to the voltage-displacement graphs were used to convert QPD outputs to bead displacement during stiffness calibrations.

The two-photon fluorescence of the red fluorescent beads increases with the trapping laser power. Moreover, it has been shown that the axial position of the laser beam changes with the laser power as a result of laser-induced thermal expansions in the microscope objective,[84] affecting the position calibration. For the case of particles with strong two-photon absorption/emission, the laser power related difference in the calibration coefficients become more prominent under white light and at higher trapping laser powers as the image of the trapped particle tends to fade away with the increased fluorescence. Therefore, it is important to obtain a separate displacement-calibration curve for the QPD at each trapping laser power.

The choice between using white light and fluorescence for particle tracking is based on the specific conditions of the intended experiments. Moreover, the quality and maximum resolution of the particle tracking scheme is related to the positional SNR, which in turn depends on the characteristics of optically trapped probe and the detector's spectral sensitivity. For example, our group has used 800 nm and 1064 nm optical tweezers setups to conduct biophysical studies of cell membranes by extracting membrane tethers from cells using optically trapped particles.[28-30] The shadow cast by the membrane tether introduces large errors in position sensing under white light. To overcome this obstacle while maintaining the SNR, we use fluorescent probes with an emission band in a region where our QPD has a high spectral sensitivity (~ 600 nm). In fact, the position tracking SNR for the red fluorescent beads increases by ~8% in our system when switching from the white light mode to fluorescence. However, the emission band of the dragon green fluorescent particles used in section 3.2.1 coincides with an area of poor spectral sensitivity of our QPD, resulting in low SNR for tracking these particles in fluorescence mode. Therefore, the QPD position detection in these experiments was conducted in bright field.

1.2.2.2 Video-based Position Sensing

Images acquired by the CCD camera were spatially calibrated by imaging a micro-ruler with 10 μm spacing. Although the pixel resolution of our CCD imaging system is diffraction limited, there are a number of algorithms for spherical objects[85, 86] that can estimate the centroid of the particle to sub-pixel accuracy, thereby increasing the spatial resolutions of video particle tracking to nano-meter range.

We used the radial symmetry method developed by Parthasarathy[86] to track the position of the optically trapped particles to sub-pixel resolution. The results of the video-based position sensing are ultimately dependent on the accuracy and pixel noise levels associated with the particle tracking algorithm used. To demonstrate this matter, we adopted the Interactive Data Language (IDL) algorithm for the *centroid* method developed by Crocker and Weeks[87] for MATLAB to track the position of the beads in the same sets of CCD images used in the radial symmetry method. An example of the stiffness values calculated using the two particle tracking algorithms is provided in the results section. Since the image exiting the microscope objective was slightly diverging, the pixel calibration was sensitive to the position of microscope objective. Therefore, we performed a calibration against an in-focus micro-ruler by averaging the pixel size while the height of the stage (and therefore that of the objective) was changed in a range of 30 μm (covering the actual positions of microscope objective during stiffness calibrations).

1.2.3 Stiffness calibrations

Both the trap stiffness and the magnitude of the viscous drag force applied by the trapping medium on an optically trapped particle depend on the distance of the trapped object from the bottom of the trapping chamber.[47] The viscous drag force experienced by a particle in a moving viscous medium is given as:[36]

$$F_{drag} = \beta \cdot \nu = \frac{6\pi\eta\nu r}{1 - \frac{9}{16}(\frac{r}{h}) + \frac{1}{8}(\frac{r}{h})^3 - \frac{45}{256}(\frac{r}{h})^4 - \frac{1}{16}(\frac{r}{h})^5} \tag{1.1}$$

where β (kg/s) is the drag coefficient, r (m) is the radius of the bead, ν (m/s) is the fluid velocity, and h (m) is the height of the bead from the bottom of the dish.

The displacement of the laser focus in the trapping media resulting from axial displacements of the microscope objective (along the propagation axis of the trapping beam) was calibrated using the PZT stage. Prior to each experiment, the trapped bead was brought in contact with the cover slip by moving the tapping chamber in the axial (z) direction, and then raised by 16 and 30 μm above the cover slip using the PZT for experiments with the 4 and 8 μm beads, respectively. As V_S remained unchanged in the span of data collection for each experiment (30 s), the position of the trapped bead along the laser propagation axis was assumed to remain constant. Minor axial displacement of the bead within the Raleigh depth of focus (DOF) of our system was neglected since at the height of 30 μm above the cover slip it could only contribute to 0.03% change in the drag coefficient, β.

1.2.3.1 Active stiffness calibration based on viscous drag force method

Forces applied on a microsphere in the proximity of the trapping chamber's bottom can be calculated using Eq. (1.1). Holding the trapped bead at a constant height above the cover slip, we moved the PZT stage at controlled velocities to induce known viscous forces on the optically trapped microsphere based on Eq. (1.1). Displacement of the bead from the center of the trap was recorded as a differential voltage by the QPD. These voltages were converted to displacements using the voltage-displacement equations. The resulting data for displacement-force graph were linearly fitted for small displacements from the center of the trap (<1 μm) using $f = -k \cdot x$, where the stiffness of the trap (k) is extracted from the slope of the fit.

1.2.3.2 Passive stiffness calibration method based on power spectral density (PSD) method

The Brownian motion of a particle in an optical trap can be described by Langevin equation. For particles in fluids with low Reynolds numbers, the power spectrum of the Brownian motion is a Lorentzian function:

$$S(f) = \frac{K_B T}{\pi^2 \beta (f^2 + f_0^2)} \tag{1.2}$$

where f (Hz) is frequency, and f_0 is the roll-off frequency of the Lorentzian curve. Parameter f_0 can be extracted by plotting the PSD of the Brownian motion of the bead, and is then used to calculate the stiffness (k) of the optical trap (in either x or y direction) knowing the hydrodynamic drag coefficient β as:

$$k = 2\pi\beta f_0 \tag{1.3}$$

The position sensing method used in this approach should be able to acquire data at frequencies that are considerably higher than the optical trap's roll-off frequency. Position samplings at 10 kHz - 50 kHz are commonly reported in the literature. Although high-speed cameras along with algorithms that account for the aliasing and blur artifacts intrinsic to camera position sensing have been implemented in studying the PSD of an optical trap,[45, 88, 89] the use of such apparatus in the absence of multiple or drifting optical traps is not common. Instead, high bandwidth non-video position sensing is commonly employed for stiffness calibration using PSD at a higher accuracy and a lower equipment cost. Our video position sensing system cannot be used to study the full spectrum of the PSD since its acquisition frequency (179 Hz) is well below the roll-off frequency of our

optical trap. For stiffness calibration using the PSD method, we used the QPD position data recorded at 50 kHz. A MATLAB application developed by Tolic-Nørrelykke et al.[42] was used to accurately extract the roll-off frequency with results discussed in section 3.

1.2.3.3 Passive Stiffness Calibration Based on Equipartition Theorem Method

Equipartition theorem assumes $0.5K_BT$ of thermal energy for each degree of freedom where K_B is the Boltzmann constant (≈ 1.38x10^{-23} J K^{-1}), and T (K) is the absolute temperature. On the other hand, energy associated with thermal fluctuations of a particle in an optical trap with stiffness (k_x) in x direction equals $0.5k_x\langle x^2\rangle$ where $\left\langle x^2\right\rangle$ is the position variance of the trapped particle in the x direction. By calculating the position variance of the trapped bead, we can measure the trap stiffness along the x axis (k_x) as:

$$k_x = K_B T\left\langle x^2\right\rangle^{-1} \tag{1.4}$$

Similarly, we can measure the trap stiffness in the y direction (k_y) using the particle position variance along the y axis. This method of determining the trap stiffness requires a calibrated position sensing device, but does not require calculating the drag coefficient of the trapped bead, or knowing the viscosity of the trapping medium. We recorded the position of the bead in the trap using the CCD camera, with stiffness calibration results presented in section 3.

1.2.3.4 Passive Stiffness Calibration Based on Boltzmann Statistics Method

In the classical Boltzmann statistics approach, the trapped particle's position histogram is assumed to have a normal distribution resulting from a Gaussian trapping laser beam. In

thermal equilibrium, Boltzmann statistics describes the probability density $p(x)$ of the particle position as a function of the optical trap's potential $E(x)$:[58]

$$p(x)dx = Ce^{-\frac{E(x)}{K_B T}} \tag{1.5}$$

where C is a normalization factor. Normalized histogram of the particle's positions in the optical trap is used to calculate the potential energy function:

$$E(x) = -K_B T \ln p(x) + K_B T \ln C \tag{1.6}$$

The contribution of dx is incorporated in C, the normalization factor, and represented in the second term in Eq. (1.6). This term is an energy offset, and is neglected by assuming zero potential at the center of the optical trap. To determine the potential energy, the logarithm of the function fitted to the calculated distribution of particle positions is taken and multiplied by $-K_B T$. The resulting distribution is fitted by a quadratic equation $E(x) = \frac{k_x}{2}x^2 + c$ where k_x is the trap stiffness along the x axis, and c is an energy offset assumed to be zero. The trap stiffness along y axis is measured in the same way as that of along the x axis.

By assuming a normal distribution for the trapped particle's position histogram and fitting a parabola to the logarithm of the normal distribution, the results calculated by the Boltzmann statistics method become identical to those by the Equipartition theorem. In theory, this approach can enhance the reconstruction of the optical trap potential by relying on the wings of the position histogram. However, this advantage is absent in practice due to the relatively small counts in the wings of the histogram (especially in higher trapping laser powers), rendering them as sources of additional uncertainty.

Moreover, the spatial mode of the trapping laser may be perturbed by other modes at high laser output powers, resulting in a non-Gaussian energy distribution across the diameter of the optical trap.

Therefore, we modified the Boltzmann statistics approach by fitting the trapped particle's position histogram using a Kernel function with a smoothing bandwidth of approximately 1 nm instead of a Gaussian function. We then numerically took the logarithm of the function fitted to the calculated distribution of particle positions and multiplied it by $-K_B T$. Instead of fitting the resulting potential distribution function with a parabola, we numerically took the position derivative of the energy function. The trap stiffness was measured from the slope of a linear fit to the resulting displacement-force distribution over a region equivalent to one standard deviation away from the center of the trap where a linear distribution was generally observed. We present the stiffness calibration results of the modified Boltzmann statistics approach in section 3. Calibrating an optical trap using the Boltzmann method does not require knowing the trapped particle's shape, drag coefficient, or medium's viscosity. We applied the Boltzmann statistics calibration method to the same position data sets recorded for the equipartition theorem calibration method using the CCD camera.

1.3 Results

1.3.1 Displacement calibrations

1.3.1.1 QPD-based position sensing

Bead movements with steps as small as 10 nm were resolvable by the QPD. Voltage-displacement curves showed a linear QPD response for bead displacements smaller than 1 μm from the center of the optical trap.

Normalizing the differential voltage of the *x* and *y* channels by V_S did not improve the linear fits to the voltage-displacement data, mainly due to the absence of large axial displacements. While normalization decreases the susceptibility of linear fits to ambient optical noise, it also makes the slope of the fit dependent on background brightness. Therefore, in controlled experimental environments like ours with negligible changes in the background signal and the trapped particle's axial displacement, using the single differential voltages V_x and V_y (as opposed to normalized QPD outputs) is preferred.

The QPD displacement calibration coefficients for the 4 and 8 μm green fluorescent beads respectively changed by 8% and 4% under the fluorescence mode over the range of trapping laser powers in this study. These coefficient changes increase to 19% and 6% for the 4 and 8 μm green fluorescent beads under the white light, respectively. For the case of the 4 μm red fluorescent beads, the QPD displacement calibration coefficients vary over the trapping laser powers by 22% in fluorescence mode and 37% in the bright field mode. While we did not use the normalized QPD outputs, it should be noted that in all cases, normalization of the differential QPD voltages by V_S decreased the dependency of

the displacement calibration coefficient on the trapping laser power in an arbitrary manner but did not eliminate it.

1.3.1.2 Video-based position sensing

Pixel calibration resulted in 158 nm/pixel in both *x* and *y* directions. The bead's centroid position was estimated with sub-pixel accuracy using the particle tracking algorithms. Data recorded from a stationary 4 μm bead attached to a cover slip showed a displacement noise of ~ 0.03 pixels for the radial symmetry and 0.06 pixels for the centroid methods corresponding to 4.7 and 9.5 nm, respectively. This value was measured as 0.042 pixels for the 8 μm beads using the radial symmetry method, corresponding to 6.6 nm.

1.3.2 Stiffness calibrations

Each of the calibration methods discussed in this report calibrate the optical trap's transverse stiffness through the same procedure for both *x* and *y* directions. The results in the *y* direction followed the same trends as the results in the *x* direction in all calibration methods. Since the goal of this study is to provide a side-by-side comparison between the stiffness calibration methods, and for simplicity, we only present trap stiffness measured by each calibration approach in only one of the principle directions, *x*.

1.3.2.1 Active stiffness calibration method based on viscous drag force

In Fig. 1.2, we present the optical trap stiffness for the 4 and 8 μm beads as a function of laser power delivered to the specimen plane using the active stiffness calibration method

based on application of viscous drag force. Each point in the graph is extracted from the slope of a linear fit to the displacement-force graph obtained at the corresponding laser power (Fig. 1.2 inset). The stiffness values of our optical trap for the 4 μm beads ranged from 63.7 ± 2.9 pN.μm^{-1} at 51 mW to 771.1 ± 69.9 pN.μm^{-1} at 1.38 W while the stiffness values for the 8 μm beads ranged from 51.6 ± 8.5 pN.μm^{-1} at 51 mW to 733.8 ± 78.8 pN.μm^{-1} at 1.38 W. As expected, a linear increase in optical trap stiffness was observed for both beads as the laser power increased. If not accounted for, the laser-induced temperature increase results in an over-estimation of optical trap stiffness, which progressively increases with trapping power.

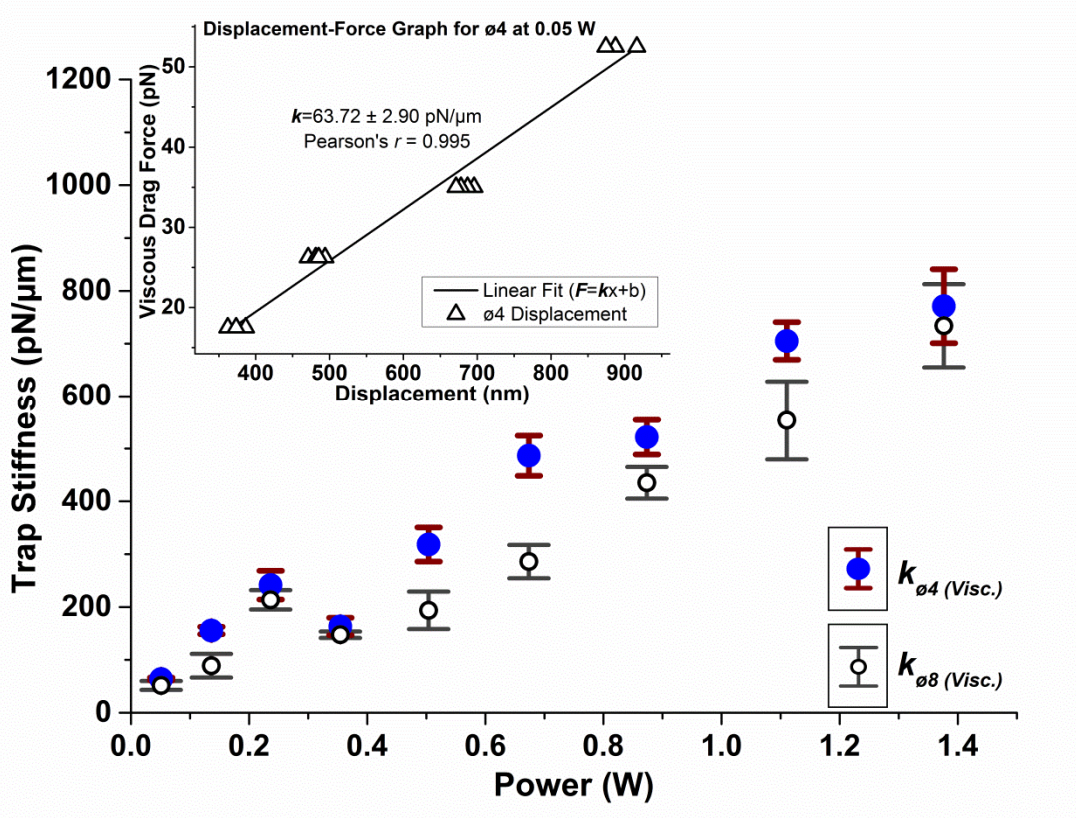

Fig. 1.2 Trap stiffness as a function of laser power at the specimen plane, using the active calibration method based on application of viscous drag force. The $k_{ø4\ (Visc.)}$ data points (represented as larger filled circles) and $k_{ø8\ (Visc.)}$ data points (represented as smaller unfilled circles) correspond to the estimated stiffness values of 4 µm red and 8 µm green fluorescent beads, respectively. The inset shows a typical displacement-force graph for the 4µm red beads at 0.05 W. The ø4 data points (shown as unfilled triangles) represent bead displacements from the center of the trap resulting from calculated viscous drag forces. The error bars to the mean estimated stiffness values using the red and green fluorescent beads are represented by thick vertical lines with short horizontal caps and thin vertical lines with long horizontal caps, respectively.

The average standard deviations from the mean stiffness values measured for the 4 µm bead is 7.6%. The average standard deviation increases to 12.7% for the 8 µm bead. These values are comparable to the uncertainties in the particle sizes (5% and 8.75% for

the 4 and 8 μm beads, respectively). The large Pearson's r value (0.995) of the linear fit to the displacement-force graphs show that the optical trap behaves as a linear spring for bead displacements smaller than 1 μm (Fig. 1.2 inset). Thus, optical trap stiffness calibration based on viscous drag force does not suffer the theoretical or numerical approximations in modeling the optical trap behavior associated with the other calibration approaches used in this study.

The viscous drag force calibration method reports stiffness values for the 8 μm beads that are on average 23% less than those of the 4 μm beads across the laser powers used in this study. The stiffness values are directly extracted from the displacement-force graphs involving controlled external forces and report the smallest standard deviations compared to the other calibration methods used in this study. Therefore, we regard the trap stiffness calculated using the viscous drag force method as the most accurate and reproducible optical trap stiffness values in our experiments.

We repeated the trap stiffness calibrations in samples consisting of the 4.2±0.21 μm red fluorescent beads and the 4.18±0.4 μm green fluorescent beads to investigate the effect of two-photon absorption on the measured stiffness. Figure1.3 shows the results of the trap stiffness calibrations using the viscous drag force method over the low, mid, and high laser powers for both beads. The $k_{\varnothing 4R\ (Visc.)}$ and $k_{\varnothing 4G\ (Visc.)}$ data points correspond to the estimated stiffness values of 4 μm red and 4 μm green beads under white light, respectively. The difference between the mean stiffness values calculated using the two beads at each trapping laser power was smaller than the sum of standard deviations to the means, and ranged from 10.6% at 51 mW to < 0.01% at 1.38 W. Thus, the effects of two-

photon absorption on the optical forces and the measured stiffness using particles in this volume-scale are negligible.

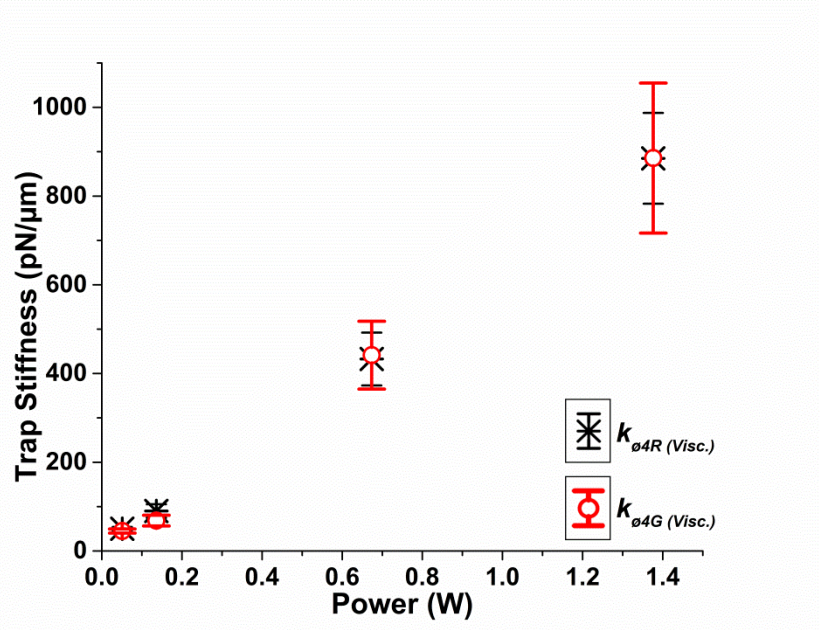

Fig. 1.3 Trap stiffness as a function of laser power at the specimen plane, using the active calibration method based on application of viscous drag force. The $k_{ø4R\ (Visc.)}$ data points (represented as asterisks) and $k_{ø4G\ (Visc.)}$ data points (represented as circles) correspond to the estimated stiffness values of 4 μm red and 4 μm dragon green beads under white light, respectively. The error bars to the mean estimated stiffness values using the red and dragon green fluorescent beads are represented by thin vertical lines with short horizontal caps and thick vertical lines with long horizontal caps, respectively.

1.3.2.2 Passive static calibration based on power spectral density method

To find the characteristic roll-off frequency (f_0) of the optical trap, we recorded the position of 10 sequentially trapped beads of either diameter at various laser powers at a sampling rate of 50 kHz. We analyzed the PSD of bead displacements using an application developed by Tolic-Nørrelykke et al.[42] Data sets recorded for 10 s, and cropped at 5 s and 2 s yielded the same roll-off frequencies. The roll-off frequencies for

the experiments using the 4 μm beads were measured in the range of 255.6 ± 66 Hz at a trapping laser power of 51 mW to 1422 ± 256 Hz at 504 mW. The roll-off frequencies using the 8 μm beads were measured to range from 195 ± 30.3 Hz at 51 mW to 830.1 ± 64.9 Hz at 504 mW. Taking the effects of laser-induced temperature increase into consideration, these roll-off frequencies correspond to stiffness values in the range of 60.2 ± 16 $pN.\mu m^{-1}$ at 51 mW to 276.6 ± 39.1 $pN.\mu m^{-1}$ at 504 mW for the 4 μm beads, and 40.3 ± 7.9 $pN.\mu m^{-1}$ at 51 mW to 161.5 ± 11 $pN.\mu m^{-1}$ at 504 mW for the 8 μm beads.

Figure1.4 shows the optical trap stiffness calculated for the 4 and 8 μm particles using the PSD method. The correlation between the trap stiffness and laser powers is linear up to the trapping laser power of 504 mW. However, at higher trapping powers, the uncertainty in the estimated stiffness values by the PSD calibration method increases, with reduced sensitivity of the stiffness estimates to power increments and deviation from a linear trend. This observation is in agreement with the previous reports that employed this stiffness calibration method.[78] The maximum laser trapping power range at which the PSD calibration method could be used to estimate reproducible stiffness calibration results was higher than the other two passive calibration methods as shown in the next section, but lower than the active stiffness calibration method. Within this range, the PSD method reports stiffness values for the 8 μm bead that are on average 42% smaller than those reported for the 4 μm bead. The average standard deviations from the mean stiffness values calculated for the 4 and 8 μm beads using the PSD method were 18% and 12%, respectively.

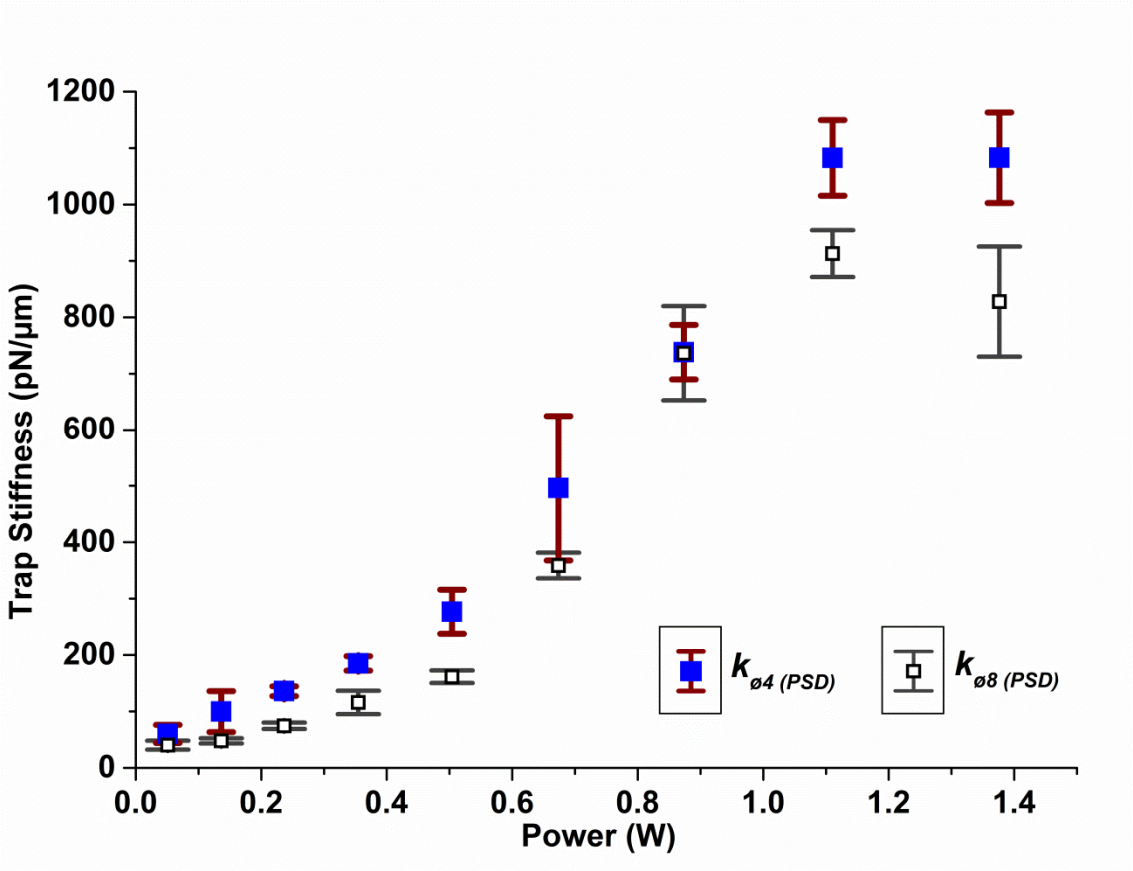

Fig. 1.4 Trap stiffness as a function of laser power at the specimen plane, using the passive stiffness calibration method based on the power spectral density. The $\boldsymbol{k}_{ø4\ (PSD)}$ data points (represented as larger filled squares), and $\boldsymbol{k}_{ø8\ (PSD)}$ data points (represented as smaller unfilled squares) correspond to the estimated stiffness values of red 4 µm and green 8 µm beads, respectively. The standard deviation from the mean measured stiffness values using the red and green fluorescent beads at each trapping laser power are represented by thick vertical lines with short horizontal caps, and thin vertical lines with long horizontal caps, respectively.

1.3.2.3 Passive stiffness calibration based on equipartition theorem

Using the variance of bead displacements as observed by the camera, the optical trap stiffness values for the 4 µm beads were estimated in the range of 36.8 ± 7.5 pN.µm^{-1} at 51 mW of trapping laser power in the focal plane, to 192 ± 59.6 pN.µm^{-1} at 355 mW. The

stiffness values for the 8 μm beads were estimated in the range of 38.9 ± 18 pN.μm^{-1} at 51 mW to 196.5 ± 64.6 pN.μm^{-1} at 355 mW (Fig. 1.5a). The trap stiffness calculated by the Equipartition theorem is in good agreement with the stiffness measured using the other methods at lower trapping laser powers. While video particle tracking at 179 fps was able to measure the optical trap stiffness using the equipartition theorem at trapping laser powers of up to 355 mW and observe a linear increase in the measured trap stiffness versus laser power, the method lost sensitivity to the increments in the trapping laser power beyond 355 mW and no consistent results were reported at higher laser powers (Fig. 1.5b).

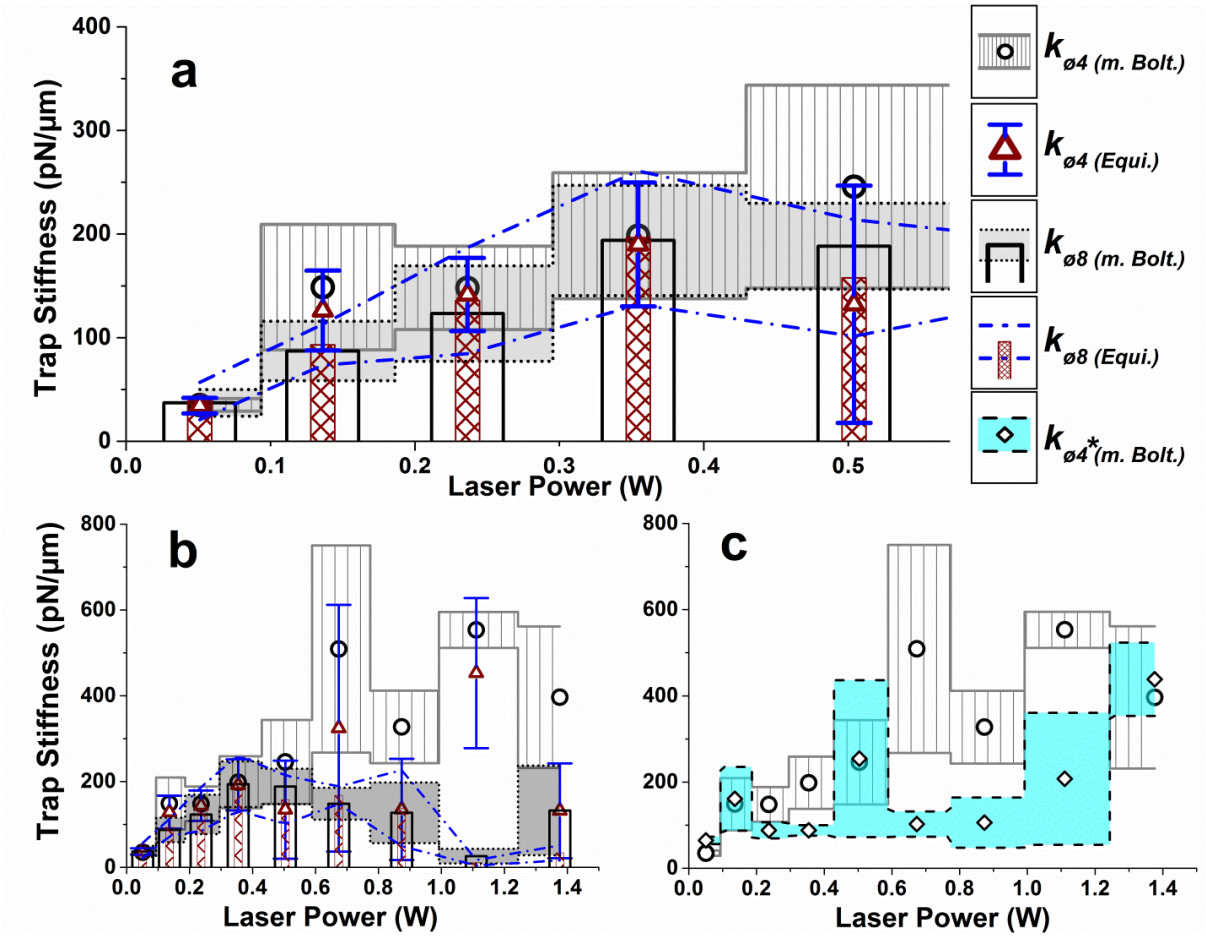
a
b
c
Trap Stiffness (pN/μm)
Laser Power (W)
$k_{ø4\ (m.\ Bolt.)}$
$k_{ø4\ (Equi.)}$
$k_{ø8\ (m.\ Bolt.)}$
$k_{ø8\ (Equi.)}$
$k_{ø4^{*}(m.\ Bolt.)}$

Fig. 1.5 Trap stiffness as a function of laser power at the specimen plane for 4 and 8 μm beads, using passive stiffness calibration methods based on the Boltzmann statistics and the Equipartition Theorem. The $\boldsymbol{k}_{\varnothing 4\ (m.\ Bolt.)}$ data points (represented as circles), and $\boldsymbol{k}_{\varnothing 4\ (Equi.)}$ data points (represented as triangles) correspond to the estimated stiffness values for the 4 μm beads using the modified Boltzmann statistics and the Equipartition Theorem, respectively. The $\boldsymbol{k}_{\varnothing 8\ (m.\ Bolt.)}$ data points (represented as unfilled columns) and $\boldsymbol{k}_{\varnothing 8\ (Equi.)}$ data points (represented as shaded columns) correspond to the estimated stiffness values for the 8 μm beads using the modified Boltzmann statistics and the Equipartition Theorem methods, respectively. Particles in the aforementioned data sets were tracked using the radial symmetry method. The $\boldsymbol{k}_{\varnothing 4^*\ (m.\ Bolt.)}$ data points (represented as diamonds) correspond to the estimated stiffness values for the 4 μm beads using the same particles images and calibration methods as in $\boldsymbol{k}_{\varnothing 4\ (m.\ Bolt.)}$, but with the centroid method used to track the optically trapped particles. The standard deviation from the mean measured stiffness values at each trapping laser power is shown as error bars. The error bars to the estimated stiffness values $\boldsymbol{k}_{\varnothing 4\ (m.\ Bolt.)}$,$\boldsymbol{k}_{\varnothing 4\ (Equi.)}$, and $\boldsymbol{k}_{\varnothing 4^*\ (m.\ Bolt.)}$ are represented by solid horizontal lines, capped vertical lines, and dashed horizontal lines, respectively. The error bars to the estimated stiffness values$\boldsymbol{k}_{\varnothing 8\ (m.\ Bolt.)}$ and $\boldsymbol{k}_{\varnothing 8\ (Equi.)}$ are represented by dotted horizontal lines and a dash-dot spline, respectively. (a) Stiffness values $\boldsymbol{k}_{\varnothing 4\ (m.\ Bolt.)}$, $\boldsymbol{k}_{\varnothing 4\ (Equi.)}$, $\boldsymbol{k}_{\varnothing 8\ (m.\ Bolt.)}$, and $\boldsymbol{k}_{\varnothing 8\ (Equi.)}$ at lower trapping laser powers (0.05-0.55 W). (b) Stiffness values$\boldsymbol{k}_{\varnothing 4\ (m.\ Bolt.)}$, $\boldsymbol{k}_{\varnothing 4\ (Equi.)}$, $\boldsymbol{k}_{\varnothing 8\ (m.\ Bolt.)}$, and $\boldsymbol{k}_{\varnothing 8\ (Equi.)}$ over an extended range of trapping laser powers (0.05-1.5 W). Neither of the approaches produced reliable stiffness results at trapping laser powers above 0.5 W. (c) Dependence of the measured trap stiffness on the particle tracking algorithm.

Optical trap stiffness calibration methods based on measuring the Brownian displacements of an optically trapped particle are highly dependent on accurate position sensing, and easily disturbed by the presence of displacement noise. The accuracy of the stiffness values reported by this statistical calibration approach can be improved at higher trapping laser powers by enhancing the position detection's spatial and temporal resolution. Estimated optical trap stiffness by the Equipartition theorem method has a direct correlation with the absolute temperature of the trapping medium (Eq. 1.4). The estimated 2.83 K temperature increase at 355 mW attributes to less than 1% under-estimation of stiffness if the laser-induced temperature increase is neglected. The Equipartition theorem calibration method reports stiffness values for the 8 μm bead that are on average 6% smaller than those reported for the 4 μm bead in its effective range of 50-355 mW. The average standard deviations from the mean stiffness values calculated using the Equipartition theorem over this range are 26% and 34% for the 4 and 8 μm beads, respectively. Therefore, we regard the Equipartition theorem as a less accurate method in calibrating optical trap stiffness as compared to the PSD and viscous drag force methods.

1.3.2.4 Passive stiffness calibration based on Boltzmann statistics method

In Fig. 1.5, optical trap stiffness values, estimated by the modified Boltzmann statistics calibration method using the CCD camera as position sensing means, are presented as a function of trapping laser powers in the focal plane. Estimated optical trap stiffness values for the 4 μm beads ranged from 35 ± 6.1 $pN.\mu m^{-1}$ at 51 mW to 198.3 ± 60.7

pN.μm^{-1} at 355 mW. The stiffness values for the 8 μm beads ranged from 37.1 ± 12.9 pN.μm^{-1} at 51 mW to 193.8 ± 53.2 pN.μm^{-1} at 355 mW. The average standard deviations from the mean stiffness values calculated using the modified Boltzmann statistics method over this range are 29% and 33% for the 4 and 8 μm beads, respectively. The trap stiffness measurements by the Equipartition theorem and the modified Boltzmann statistics calibration methods for the 4 and 8 μm beads over the trapping laser power range of 50-504 mW are presented in Fig. 1.5a for comparison. Both calibration methods are capable of observing the size-dependent differences in optical trap stiffness within their effective range. However, the average difference of 6% between the measured stiffness for the 4 and 8 μm beads using the Equipartition theorem increases to 13.6% when using the modified Boltzmann statistics method.

The average standard deviation from the mean calculated stiffness values did not change in a meaningful way between the two methods. This suggests that the decreased dependency of the stiffness calculations on the wings of the particle's position distribution in the modified Boltzmann statistics method does not introduce significant uncertainties in the calculated results. In turn, the discrepancies between the two methods become apparent as the trapping laser powers increase, resulting in fewer data points in the far bins of the trapped particles' position histogram. The classical Boltzmann statistics approach becomes limited in performance at 355 mW while the modified Boltzmann statistics method allows for the measurements to be extended into a higher laser power of 504 mW for the 4 μm beads, measuring a stiffness of 245.7 pN.μm^{-1}.

While the modified Boltzmann statistics also shows some improvement over the Equipartition theorem in calculating the mean stiffness value for the larger particle at 504 mW, its performance could not be reliably extended into higher powers for the 8 μm bead mainly due to the higher pixel calculation error in tracking the larger particles. The performance of any calibration method relying on video based position sensing method relies on the accuracy of the sub-pixel particle tracking algorithm used. Figure 1.5c provides an example of how the modified Boltzmann statistics approach is limited in performance using the same bead image sets as tracked by the centroid particle tracking algorithm; a tracking algorithm that provides less accuracy and larger pixel noise for sub-pixel particle tracking.[86]

The optical trap stiffness value estimated using the Boltzmann statistics method is directly related to the absolute temperature of the trapping medium (Eq. 1.6). Similar to the Equipartition theorem method, in our system the trap stiffness is under-estimated by 1.4% at the trapping power of 504 mW using the Boltzmann statistics method if laser-induced temperature increase at the focus is not accounted for.

1.4 Discussion

We summarize the results from our stiffness calibration methods at trapping laser powers ranging from 50 mW to 1.38 W in Fig. 1.6. Horizontal and vertical axes are plotted on logarithmic scales to enhance the visibility at lower powers where the measured stiffness values are in close proximity. To enhance the comparison between the trapping laser power increments and estimated stiffness changes using each calibration method, the inset shows the results of the four stiffness calibration methods but with its vertical and

horizontal axes respectively divided by the stiffness and laser power values of the smallest data points plotted (35 $pN.\mu m^{-1}$ for the modified Boltzmann statistics method using the 4 μm bead at 50 mW). The results of each stiffness calibration method are considered reliable within the trapping laser power range where a linear increase in the trap stiffness with increasing laser power is estimated. Discrepancies exist between the methods in the trap stiffness values reported at a given trapping laser power, the slope of their stiffness *vs.* laser power, and the sensitivity of each approach in observing the size dependent optical trap stiffness changes. While the trap stiffness estimated by all calibration methods are in good agreements at lower trapping laser powers, discrepancies between the methods become more apparent at higher trapping laser powers.

Extrapolation of the power-stiffness fits in Fig. 1.6 reveals non-zero stiffness values at zero trapping power. Optical trapping is not achieved until the optical forces experienced by the particle surpass the forces exerted on the particle by random collisions of the trapping medium. Zero stiffness as measured by the Equipartition theorem indicates that the position variance of the particle approaches infinity. In Boltzmann statistics, a flat position histogram is required to assume zero stiffness. Neither of these cases is realized in practice given the limited spatial range of the position sensing devices and the limited duration of the observations. In the viscous drag force approach where the optical trap is modeled by Hooke's law, zero stiffness is realized if infinitesimally small forces result in infinitely large movements. This is not achieved since even in the absence of the trapping laser, frictional forces counter the free diffusion of the particle in the trapping medium.[90]

While these physical constraints restrict the measurement of zero stiffness at zero trapping laser power, position sensing errors are mainly responsible for the residual values measured by extrapolating the power-stiffness (or displacement-force) fits towards the origin. Minor position calibration errors and noise can lead to an overall under (or over) estimation of trap stiffness at each power, giving rise to residual stiffness values at zero trapping laser power. Similarly, small imperfections in the alignment of the position sensing device with the center of the trap will result in measuring residual forces at zero displacement, in both the viscous drag force and Boltzmann statistics methods. At low trapping laser powers, position sensing noise shifts the displacement-force graph in the positive direction of the displacement axis resulting in apparent negative residual forces. At higher trapping laser powers, the increased scattering force results in an axial displacement of the particle when lateral forces are applied.[91] This axial displacement is not bi-lateral and occurs along the coma axis,[74] resulting in a small lateral bias in measuring bead's displacements. This in turn shifts the force-displacement graph upwards resulting in an increased apparent residual force at zero displacement.

Laser-induced temperature increase was considered in estimating all of the results presented in Fig. 1.6. Not accounting for the temperature increase at higher laser powers results in under-estimating the trap stiffness when using the Equipartition theorem and Boltzmann statistics calibration methods, and over-estimating the stiffness in PSD and viscous drag force calibration approaches. Increases in the absolute temperature of the trapping media is directly associated with increases in the stiffness value estimated by Equipartition theorem and Boltzmann statistics calibration methods. However, increased

temperature of the trapping media is directly associated with decreases in the stiffness values estimated by the viscous drag and PSD calibration methods because of the inverse effect of temperature with the dynamic viscosity of the trapping media and drag coefficient, β.

The sensitivity of the stiffness calibration methods to the effects of temperature increase depends on the thermal characteristics of the trapping medium and the trapping laser power range. In our case, we assumed a temperature increase of 8 K/W for our DI water trapping medium. Given the small contribution of bead properties to the laser-induced heating in optical traps,[78] the low absorption of water at 1064 nm, and the range of laser power used, this assumption remains acceptable for the purpose of our comparative study of stiffness calibration methods. Moreover, a 50% error in this assumption (8±4 K/W) does not change the overall trend of the results and changes the measured stiffness by 0.1-1.9% using the Equipartition and Boltzmann statistics methods, and 0.5-11% using the Viscous drag force and PSD methods over the range of laser powers used in this study. Results of the PSD and viscous drag force calibration methods were more sensitive to the temperature increments compared to those of the Equipartition theorem and Boltzmann statistics calibration methods. This is due to the larger temperature-induced changes in water's dynamic viscosity (20.6% decrease) compared to the absolute temperature change (3.6% increase) within the laser power range used in our study.

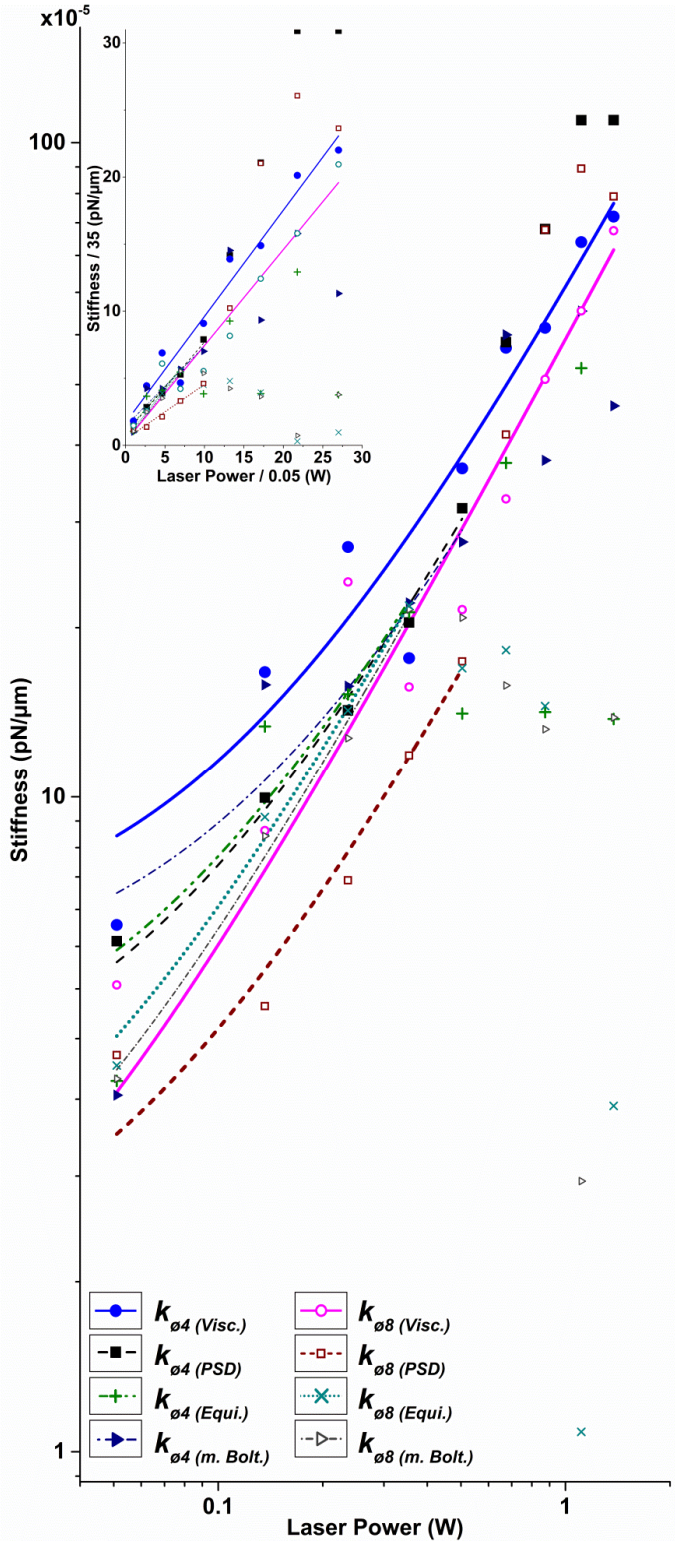
x10-5
100
10
1
Stiffness (pN/μm)
0.1
1
Laser Power (W)
Stiffness / 35 (pN/μm)
Laser Power / 0.05 (W)
k ø4 (Visc.)
k ø4 (PSD)
k ø4 (Equi.)
k ø4 (m. Bolt.)
k ø8 (Visc.)
k ø8 (PSD)
k ø8 (Equi.)
k ø8 (m. Bolt.)

Fig. 1.6 Summary of the results of four stiffness calibration methods using beads with two different mean diameters (4 μm and 8 μm). Horizontal and vertical axes are plotted in logs to enhance the visibility at lower powers where the measured stiffness values are in close proximity. Stiffness values $\boldsymbol{k}_{\varnothing 4\ (Visc.)}$ and $\boldsymbol{k}_{\varnothing 8\ (Visc.)}$ were measured using the viscous drag force calibration and are represented as filled circles and unfilled circles, respectively. The $\boldsymbol{k}_{\varnothing 4\ (PSD)}$ and $\boldsymbol{k}_{\varnothing 8\ (PSD)}$ data sets (represented as filled squares and unfilled squares, respectively) correspond to stiffness results estimated using the power spectral density method. The results of the Equipartition Theorem stiffness calibration method, $\boldsymbol{k}_{\varnothing 4\ (Equi.)}$ and $\boldsymbol{k}_{\varnothing 8\ (Equi.)}$, are represented with plus and cross signs, respectively. The results of the Boltzmann statistics method, $\boldsymbol{k}_{\varnothing 4\ (m.\ Bolt.)}$ and$\boldsymbol{k}_{\varnothing 8\ (m.\ Bolt.)}$, are represented with rightward pointing filled triangles and rightward pointing unfilled triangles, respectively. The linear fits to the estimated stiffness values using the viscous drag force calibration methods, $\boldsymbol{k}_{\varnothing 4\ (Visc.)}$ and $\boldsymbol{k}_{\varnothing 8\ (Visc.)}$, are represented as thick solid lines. The linear fits to the estimated stiffness values using the power spectral density method, $\boldsymbol{k}_{\varnothing 4\ (PSD)}$ and $\boldsymbol{k}_{\varnothing 8\ (PSD)}$, are represented as a dashed line and a short-dash line, respectively. The linear fits to the estimated stiffness values using the Equipartition Theorem calibration method,$\boldsymbol{k}_{\varnothing 4\ (Equi.)}$ and $\boldsymbol{k}_{\varnothing 8\ (Equi.)}$, are represented by a dash-dot-dot and a dotted line, respectively. The linear fits to the estimated stiffness values using the Boltzmann statistics method, $\boldsymbol{k}_{\varnothing 4\ (m.\ Bolt.)}$ and $\boldsymbol{k}_{\varnothing 8\ (m.\ Bolt.)}$, are represented by a dash-dot and a short dash-dot, respectively. The inset shows the results of the four stiffness calibration methods but with its vertical and horizontal axes divided by the stiffness and laser power values of the smallest data points plotted (35 $pN.\mu m^{-1}$ and 0.05 W, respectively) to enhance the comparison between the trapping laser power increments and estimated stiffness changes using each calibration method.

QPD and other non-video position sensing devices offer nanometer spatial resolution at kHz sampling frequencies, but to achieve their highest spatial resolution often requires superluminescence or laser illumination, which entails special optics and careful alignment and calibration. In return, at a lower cost compared to high-speed cameras, the QPD can be used to characterize optical traps in studies involving high trapping laser powers. We used the QPD in an imaging configuration which offers less spatial resolution than the back focal plane interferometry configuration. The limited spatial and temporal resolution of position sensing is the limiting factor in the efficiency of calibration methods at higher trapping laser powers. Any enhancement of the position sensing accuracy and precision will in turn enhance the efficiency of the stiffness calibration methods.

Cameras with low pixel noise can offer nanometer spatial resolution for simultaneous tracking of multiple objects in conjunction with sub-pixel particle tracking algorithms. At a comparable cost to the non-video position sensing means, cameras with native acquisition rates of several hundred fps can be used at a few kHz frame rates through binning. This frame rate is sufficient to perform frequency analysis of the thermal fluctuations of large optically trapped particles.[92] However, high speed CMOS sensors and line scan cameras are still required to achieve a comparable temporal resolution offered by the non-video position sensing means (tens of kHz) needed for particles in the Rayleigh regime. Currently, these ultra-fast video position sensing schemes are often costly and limited in performance compared to their non-video counter parts. However, common video acquisition rates of >100 Hz can be used to determine the stiffness of an

optical trap in most biophysical application where the trapping laser power is limited to prevent optical damage to the samples.

Stiffness calibration methods using the Equipartition theorem and Boltzmann statistics measure the thermal vibrations of a trapped particle to estimate the trap stiffness. In the Equipartition theorem method, position variance is directly used to estimate the stiffness whereas Boltzmann statistics calibration method reconstructs a normalized probability function based on the distribution of trapped particle's positions in the optical trap to measure the stiffness. Thus, Boltzmann statistics method is less sensitive to the white noise in the measurement instrumentation which when using the Equipartition theorem can cause under-estimation of the trap stiffness by adding to the apparent variance of the particle position. The statistical nature of the Boltzmann method enhances the spatial resolution of the system in reconstructing the probability function of the trapped particle's position.

The Equipartition theorem method requires the least amount of post processing for calibrating the stiffness of an optical trap compared to the other methods in this study. Since the position variance is a biased (always positive) estimator, the Equipartition theorem is more sensitive to the position detection noise, detector's spatial and temporal resolution, and detector's position calibration errors compared to the other calibration methods. This bias decreases the usefulness of the Equipartition theorem calibration method when non-video position sensing means with intrinsic high frequency noise are used. This issue can be addressed by low-pass filtering the position signal, but care must

be given to account for the effects of filtering parameters on the information content of the signal.[27]

Compared to the Equipartition theorem, the Boltzmann statistics method suffers less position detector related errors in estimating optical trap stiffness over the range of trapping laser powers. The Boltzmann statistics method can also be used to study the optical trap's potential energy shape. On the other hand, the probability distribution function in the Boltzmann statistics method is a continuous function fitted to discrete position data points. Therefore, the estimated optical trap stiffness values are sensitive to fitting parameters such as the bin size and the fitting function. We used a modified Boltzmann statistics approach which improved the efficiency of the method at higher trapping laser powers, and enhanced its sensitivity to particle diameter dependent variations in optical trap stiffness.

Neither the Boltzmann statistics nor the Equipartition theorem calibration methods require calculating the drag coefficient of the trapped particles, making them suitable for studies that involve trapping cell and particles of arbitrary shapes. At a given position sensing temporal and spatial resolution, both Equipartition theorem and Boltzmann statistics methods are more suitable for studying weaker optical traps with smaller optically trapped objects. Compared to the PSD and viscous drag force approaches, the Equipartition theorem and Boltzmann statistics stiffness calibration methods have a limited laser power range in which they can reliably be used to calibrate the optical trap stiffness, and offer smaller confidence in the measured stiffness.

At higher trapping powers, the viscous drag force and PSD calibration methods are more reliable for calibrating the trap stiffness. Compared to the results from other calibration methods, the PSD method has the highest sensitivity to the particle size dependent changes in trap stiffness. Studying the PSD of an optically trapped particle can also provide valuable information about the electrical and mechanical noise present in the trapping system.[93] Moreover, this method can be used to directly calibrate the position sensing device when a motorized or PZT stage is not available,[94] as well as extracting the drag coefficient for trapped particles of arbitrary shapes.[57]

Discrete numerical methods used in the PSD estimation affect the Lorentzian shape of the PSD. The low-pass effect of the position sensing diodes as well as a number of other physical and theoretical approximations[41] can affect the accuracy of the apparent roll-off frequency. Free software packages are developed and are available online that can be used to compensate for these factors[42, 95, 96] when calibrating an optical trap stiffness using the PSD method. Although the position sensing device needs not to be displacement-calibrated when using the PSD calibration method, a high spatial resolution is crucial in order to observe small thermal vibrations of the particle inside stronger optical traps, ultimately affecting the efficacy of the PSD calibration method at higher trapping laser powers.

Position detection spatial resolution is limited to nanometer range even with the most sensitive laser based position sensing schemes such as back focal plane interferometry. At higher trapping laser powers where the thermal movements of the optically trapped particle approach the spatial resolution limits of the position sensing system, active

stiffness calibration methods can produce more reliable calibration results. Controlled viscous forces (and subsequently particle displacements from the center of the trap) can be induced to overcome the low positional SNR in stronger optical traps.

Calibrating optical tweezers' stiffness using known viscous drag forces requires the most post processing effort. Accuracy of the results depends on the exact knowledge of particle size and drag coefficient, temperature and viscous properties of the medium, and having a displacement-calibrated position detection system. Motorized or PZT stages (or microfluidic trapping chambers with precise control over the flow rate) are required with active stiffness calibration methods for applying known displacements or viscous forces on optically trapped particles. In return, calibrating the optical trap against known viscous drag forces provides the most accurate and relevant stiffness results for studies involving large displacements of the trapped particle from the center of the optical trap.

1.5 References

1. A. Ashkin, "Acceleration and trapping of particles by radiation pressure," *Phys. Rev. Lett.* **24**(4), 156 (1970).

2. C. G. Baumann, V. A. Bloomfield, S. B. Smith, C. Bustamante, M. D. Wang and S. M. Block, "Stretching of single collapsed DNA molecules," *Biophys. J.* **78**(4), 1965-1978 (2000).

3. S. M. Block, D. F. Blair and H. C. Berg, "Compliance of bacterial flagella measured with optical tweezers," *Nature* **338**(6215), 514-518 (1989).

4. J. Sleep, D. Wilson, R. Simmons and W. Gratzer, "Elasticity of the red cell membrane and its relation to hemolytic disorders: An optical tweezers study," *Biophys. J.* **77**(6), 3085-3095 (1999).

5. S. Hénon, G. Lenormand, A. Richert and F. Gallet, "A new determination of the shear modulus of the human erythrocyte membrane using optical tweezers," *Biophys. J.* **76**(2), 1145-1151 (1999).

6. K. Svoboda and S. M. Block, "Biological applications of optical forces," *Annu. Rev. Biophys. Biomol. Struct.* **23**(1), 247-285 (1994).

7. M. Dao, C. T. Lim and S. Suresh, "Mechanics of the human red blood cell deformed by optical tweezers," *J. Mech. Phys. Solids* **51**(11-12), 2259-2280 (2003).

8. C. T. Lim, M. Dao, S. Suresh, C. H. Sow and K. T. Chew, "Large deformation of living cells using laser traps," *Acta Mater.* **52**(7), 1837-1845 (2004).

9. J. Dai and M. P. Sheetz, "Mechanical properties of neuronal growth cone membranes studied by tether formation with laser optical tweezers,"*Biophys. J.***68**(3), 988-996 (1995).

10. D. Choquet, D. P. Felsenfeld and M. P. Sheetz, "Extracellular matrix rigidity causes strengthening of integrin-cytoskeleton linkages," *Cell* **88**(1), 39-48 (1997).

11. M. M. Brandão, A. Fontes, M. L. Barjas-Castro, L. C. Barbosa, F. F. Costa, C. L. Cesar and S. T. O. Saad, "Optical tweezers for measuring red blood cell elasticity: Application to the study of drug response in sickle cell disease," *Eur. J. Haematol.* **70**(4), 207-211 (2003).

12. P. J. Bronkhorst, G. J. Streekstra, J. Grimbergen, E. J. Nijhof, J. J. Sixma and G. J. Brakenhoff, "A new method to study shape recovery of red blood cells using multiple optical trapping," *Biophys. J.* **69**(5), 1666-1673 (1995).

13. R. R. Huruta, M. L. Barjas-Castro, S. T. O. Saad, F. F. Costa, A. Fontes, L. C. Barbosa and C. L. Cesar, "Mechanical properties of stored red blood cells using optical tweezers," *Blood* **92**(8), 2975-2977 (1998).

14. G.-B. Liao, P. B. Bareil, Y. Sheng and A. Chiou, "One-dimensional jumping optical tweezers for optical stretching of bi-concave human red bloodcells," *Opt. Express* **16**(3), 1996-2004 (2008).

15. K. Svoboda, C. F. Schmidt, D. Branton and S. M. Block, "Conformation and elasticity of the isolated red blood cell membrane skeleton," *Biophys. J.* **63**(3), 784-793 (1992).

16. Y. Li, C. Wen, H. Xie, A. Ye and Y. Yin, "Mechanical property analysis of stored red blood cell using optical tweezers," *Colloids Surf. B* **70**(2), 169-173 (2009).

17. A. Ashkin, "History of optical trapping and manipulation of small-neutral particle, atoms, and molecules,"*IEEE J. Sel. Top. Quantum Elec.***6**(6), 841-856 (2000).

18. A. Ashkin, "Optical trapping and manipulation of neutral particles using lasers," *Proc. Natl. Acad. Sci. U.S.A.* **94**(10), 4853-4860 (1997).

19. T. L. Gustavson, A. P. Chikkatur, A. E. Leanhardt, ouml, A. rlitz, S. Gupta, D. E. Pritchard and W. Ketterle, "Transport of bose-einstein condensates with optical tweezers," *Phys. Rev. Lett.* **88**(2), 020401 (2001).

20. M. D. Barrett, J. A. Sauer and M. S. Chapman, "All-optical formation of an atomic bose-einstein condensate," *Phys. Rev. Lett.* **87**(1), 010404 (2001).

21. L. P. Ghislain and W. W. Webb, "Scanning-force microscope based on an optical trap," *Opt. Lett.* **18**(19), 1678-1680 (1993).

22. Y. Arai, R. Yasuda, K. Akashi, Y. Harada, H. Miyata, K. Kinosita, Jr. and H. Itoh, "Tying a molecular knot with optical tweezers," *Nature* **399**(6735), 446-448 (1999).

23. W. B. Richard and J. P. Miles, "Optical trapping and binding," *Rep. Prog. Phys.* **76**(2), 026401 (2013).

24. S. Khan and M. P. Sheetz, "Force effects on biochemical kinetics," *Annu. Rev. Biochem.* **66**, 785-805 (1997).

25. T. Nishizaka, H. Miyata, H. Yoshikawa, S. i. Ishiwata and K. Kinosita, "Unbinding force of a single motor molecule of muscle measured using optical tweezers," *Nature* **377**(6546), 251-254 (1995).

26. M. D. Wang, H. Yin, R. Landick, J. Gelles and S. M. Block, "Stretching DNA with optical tweezers,"*Biophys. J.***72**(3), 1335-1346 (1997).

27. K. C. Neuman and A. Nagy, "Single-molecule force spectroscopy: Optical tweezers, magnetic tweezers and atomic force microscopy," *Nat. Methods* **5**(6), 491-505 (2008).

28. Z. Li, B. Anvari, M. Takashima, P. Brecht, J. H. Torres and W. E. Brownell, "Membrane tether formation from outer hair cells with optical tweezers,"*Biophys. J.***82**(3), 1386-1395 (2002).

29. S. A. Ermilov, D. R. Murdock, F. Qian, W. E. Brownell and B. Anvari, "Studies of plasma membrane mechanics and plasma membrane-cytoskeleton interactions using optical tweezers and fluorescence imaging,"*Ann. Biomed. Eng.***40**(2), 476-480 (2007).

30. N. Khatibzadeh, S. Gupta, B. Farrell, W. E. Brownell and B. Anvari, "Effects of cholesterol on nano-mechanical properties of the living cell plasma membrane," *Soft Matter* **8**(32), 8350-8360 (2012).

31. N. Khatibzadeh, A. A. Spector, W. E. Brownell and B. Anvari, "Effects of plasma membrane cholesterol level and cytoskeleton f-actin on cell protrusion mechanics," *PLoS ONE* **8**(2), e57147 (2013).

32. A. Ashkin and J. M. Dziedzic, "Internal cell manipulation using infrared laser traps," *Proc. Natl. Acad. Sci. U.S.A.* **86**(20), 7914-7918 (1989).

33. A. G. Hendricks, E. L. F. Holzbaur and Y. E. Goldman, "Forces in intracellular transport: Calibrated optical trap recordings in living cells," *Biophys. J.* **102**(3, Supplement 1), 38a (2012).

34. R. W. Steubing, S. Cheng, W. H. Wright, Y. Numajiri and M. W. Berns, "Laser induced cell fusion in combination with optical tweezers: The laser cell fusion trap," *Cytometry* **12**(6), 505-510 (1991).

35. J. Mas, A. C. Richardson, S. N. Reihani, L. B. Oddershede and K. Berg-Sorensen, "Quantitative determination of optical trapping strength and viscoelastic moduli inside living cells," *Phys. Biol.* **10**(4), 046006 (2013).

36. H. Felgner, O. Müller and M. Schliwa, "Calibration of light forces in optical tweezers," *Appl. Opt.* **34**(6), 977-982 (1995).

37. F. Gittes and C. F. Schmidt, "Interference model for back-focal-plane displacement detection in optical tweezers," *Opt. Lett.* **23**(1), 7-9 (1998).

38. W. Singer, S. Bernet, N. Hecker and M. Ritsch-Marte, "Three-dimensional force calibration of optical tweezers," *J. Mod. Opt.* **47**(14-15), 2921-2931 (2000).

39. W. Grange, S. Husale, H.-J. Guntherodt and M. Hegner, "Optical tweezers system measuring the change in light momentum flux," *Rev. Sci. Instrum.* **73**(6), 2308-2316 (2002).

40. S. Ermilov and B. Anvari, "Dynamic measurements of transverse optical trapping force in biological applications," *Ann. Biomed. Eng.* **32**(7), 1016-1026 (2004).

41. K. Berg-Sørensen and H. Flyvbjerg, "Power spectrum analysis for optical tweezers," *Rev. Sci. Instrum.* **75**(3), 594-612 (2004).

42. I. M. Tolic-Nørrelykke, K. Berg-Sørensen and H. Flyvbjerg, "Matlab program for precision calibration of optical tweezers," *Comput. Phys. Commun.* **159**(3), 225-240 (2004).

43. B.-J. Chang, L. Hsu and S. Chi, "Rapid and simple automatic trapping-force calibration system for optical tweezers," *Opt. Eng.* **44**(11), 113603-113605 (2005).

44. N. B. Viana, A. Mazolli, P. A. M. Neto, H. M. Nussenzveig, M. S. Rocha and O. N. Mesquita, "Absolute calibration of optical tweezers," *Appl. Phys. Lett.* **88**(13), 131110-131113 (2006).

45. W. P. Wong and K. Halvorsen, "The effect of integration time on fluctuation measurements: Calibrating an optical trap in the presence of motion blur," *Opt. Express* **14**(25), 12517-12531 (2006).

46. M. Klein, M. Andersson, O. Axner and E. Fällman, "Dual-trap technique for reduction of low-frequency noise in force measuring optical tweezers," *Appl. Opt.* **46**(3), 405-412 (2007).

47. W. M. Lee, P. J. Reece, R. F. Marchington, N. K. Metzger and K. Dholakia, "Construction and calibration of an optical trap on a fluorescence optical microscope," *Nat. Protoc.* **2**(12), 3226-3238 (2007).

48. J. P. Sharpe, C. Iniguez-Palomares and R. Jimenez-Flores, "Optical tweezers force calibration using a fast-shuttering camera," in *Imaging, Manipulation, and Analysis of Biomolecules, Cells, and Tissues V*, pp. 644114-644118, SPIE, San Jose, CA, USA (2007).

49. A. Van der Horst and N. R. Forde, "Calibration of dynamic holographic optical tweezers for force measurements on biomaterials," *Opt. Express* **16**(25), 20987-21003 (2008).

50. A. Farré and M. Montes-Usategui, "A force detection technique for single-beam optical traps based on direct measurement of light momentum changes,"**18**(11), 11955-11968 (2010).

51. M. Fischer, A. C. Richardson, S. N. S. Reihani, L. B. Oddershede and K. Berg-Sørensen, "Active-passive calibration of optical tweezers in viscoelastic media," *Rev. Sci. Instrum.* **81**(1), 015103-015110 (2010).

52. N. Osterman, "Tweezpal - optical tweezers analysis and calibration software," *Comput. Phys. Commun.* **181**(11), 1911-1916 (2010).

53. W. H. Wright, G. J. Sonek and M. W. Berns, "Parametric study of the forces on microspheres held by optical tweezers," *Appl. Opt.* **33**(9), 1735-1748 (1994).

54. G. Lenormand, S. Hénon, A. Richert, J. Siméon and F. Gallet, "Direct measurement of the area expansion and shear moduli of the human red blood cell membrane skeleton," *Biophys. J.* **81**(1), 43-56 (2001).

55. R. M. Simmons, J. T. Finer, S. Chu and J. A. Spudich, "Quantitative measurements of force and displacement using an optical trap," *Biophys. J.* **70**(4), 1813-1822 (1996).

56. A. Le Gall, K. Perronet, D. Dulin, A. Villing, P. Bouyer, K. Visscher and N. Westbrook, "Simultaneous calibration of optical tweezers spring constant and position detector response," *Opt. Express* **18**(25), 26469-26474 (2010).

57. S. F. Tolić-Nørrelykke, E. Schäffer, J. Howard, F. S. Pavone, F. Jülicher and H. Flyvbjerg, "Calibration of optical tweezers with positional detection in the back focal plane," *Rev. Sci. Instrum.* **77**(10), 103101 (2006).

58. E. L. Florin, A. Pralle, E. H. K. Stelzer and J. K. Horber, H., "Photonic force microscope calibration by thermal noise analysis," *Appl. Phys. A* **66**(1), S75-S78 (1998).

59. M.-T. Wei and A. Chiou, "Three-dimensional tracking of brownian motion of a particle trapped in optical tweezers with a pair of orthogonal tracking beams and the determination of the associated optical force constants," *Opt. Express* **13**(15), 5798-5806 (2005).

60. M.-T. Wei, K.-T. Yang, A. Karmenyan and A. Chiou, "Three-dimensional optical force field on a chinese hamster ovary cell in a fiber-optical dual-beam trap," *Opt. Express* **14**(7), 3056-3064 (2006).

61. M. Ribezzi-Crivellari, J. M. Huguet and F. Ritort, "Counter-propagating dual-trap optical tweezers based on linear momentum conservation," *Rev. Sci. Instrum.* **84**(4), 043104 - 043104-043110 (2013).

62. S. B. Smith, Y. Cui and C. Bustamante, "Optical-trap force transducer that operates by direct measurement of light momentum," *Meth. Enzymol.* **361**, 134-162 (2003).

63. A. Farré, F. Marsà and M. Montes-Usategui, "Optimized back-focal-plane interferometry directly measures forces of optically trapped particles," *Opt. Express* **20**(11), 12270-12291 (2012).

64. J. P. Mills, L. Qie, M. Dao, C. T. Lim and S. Suresh, "Nonlinear elastic and viscoelastic deformation of the human red blood cell with optical tweezers," *Mech. Chem. Biosyst.* **1**(3), 169-180 (2004).

65. F. Qian, S. Ermilov, D. Murdock, W. E. Brownell and B. Anvari, "Combining optical tweezers and patch clamp for studies of cell membrane electromechanics,"*Rev. Sci. Instrum.***75**(9), 2937-2942 (2004).

66. O. M. Marago, P. H. Jones, P. G. Gucciardi, G. Volpe and A. C. Ferrari, "Optical trapping and manipulation of nanostructures," *Nature Nano* **8**(11), 807-819 (2013).

67. P. M. Hansen, V. K. Bhatia, N. Harrit and L. Oddershede, "Expanding the optical trapping range of gold nanoparticles,"*Nano Lett.***5**(10), 1937-1942 (2005).

68. A. Ashkin, "Forces of a single-beam gradient laser trap on a dielectric sphere in the ray optics regime," *Biophysical Journal* **61**(2), 569-582 (1992).

69. W. H. Wright, G. J. Sonek and M. W. Berns, "Radiation trapping forces on microspheres with optical tweezers,"*Appl. Phys. Lett.***63**(6), 715-717 (1993).

70. A. Rohrbach, "Stiffness of optical traps: Quantitative agreement between experiment and electromagnetic theory," *Phys. Rev. Lett.* **95**(16), 168102 (2005).

71. P. A. M. Neto and H. M. Nussenzveig, "Theory of optical tweezers," *Europhys. Lett.* **50**(5), 702 (2000).

72. A. Mazolli, P. A. Maia Neto and H. M. Nussenzveig, "Theory of trapping forces in optical tweezers,"*Proc. R. Soc. A***459**(2040), 3021-3041 (2003).

73. N. B. Viana, M. S. Rocha, O. N. Mesquita, A. Mazolli, P. A. Maia Neto and H. M. Nussenzveig, "Towards absolute calibration of optical tweezers," *Phys. Rev. E* **75**(2), 021914 (2007).

74. R. S. Dutra, N. B. Viana, P. A. Maia Neto and H. M. Nussenzveig, "Absolute calibration of forces in optical tweezers,"*Phys. Rev. A***90**(1), 013825 (2014).

75. K. Svoboda and S. M. Block, "Optical trapping of metallic rayleigh particles," *Opt. Lett.* **19**(13), 930-932 (1994).

76. M. Haghshenas-Jaryani, B. Black, S. Ghaffari, J. Drake, A. Bowling and S. Mohanty, "Dynamics of microscopic objects in optical tweezers: Experimental

determination of underdamped regime and numerical simulation using multiscale analysis," *Nonlinear Dyn.* **76**(2), 1013-1030 (2014).

77. K. C. Neuman and S. M. Block, "Optical trapping," *Rev. Sci. Instrum.* **75**(9), 2787-2809 (2004).

78. E. J. G. Peterman, F. Gittes and C. F. Schmidt, "Laser-induced heating in optical traps," *Biophys. J.* **84**(2), 1308-1316 (2003).

79. K. C. Neuman, E. H. Chadd, G. F. Liou, K. Bergman and S. M. Block, "Characterization of photodamage to escherichia coli in optical traps," *Biophys. J.* **77**(5), 2856-2863 (1999).

80. H. Misawa, M. Koshioka, K. Sasaki, N. Kitamura and H. Masuhara, "Three-dimensional optical trapping and laser ablation of a single polymer latex particle in water," *J. Appl. Phys.* **70**(7), 3829-3836 (1991).

81. K. Svoboda and S. M. Block, "Force and velocity measured for single kinesin molecules," *Cell* **77**(5), 773-784 (1994).

82. K. C. Vermeulen, G. J. L. Wuite, G. J. M. Stienen and C. F. Schmidt, "Optical trap stiffness in the presence and absence of spherical aberrations," *Appl. Opt.* **45**(8), 1812-1819 (2006).

83. A. Pralle, M. Prummer, E. L. Florin, E. H. K. Stelzer and J. K. H. Hörber, "Three-dimensional high-resolution particle tracking for optical tweezers by forward scattered light," *Microsc. Res. Tech.* **44**(5), 378-386 (1999).

84. M. Mahamdeh and E. Schaffer, "Optical tweezers with millikelvin precision of temperature-controlled objectives and base-pair resolution," *Optics express* **17**(19), 17190-17199 (2009).

85. Q. Tian and M. N. Huhns, "Algorithms for subpixel registration," *CVGIP* **35**(2), 220-233 (1986).

86. R. Parthasarathy, "Rapid, accurate particle tracking by calculation of radial symmetry centers," *Nat. Meth.* **9**(7), 724-726 (2012).

87. J. C. Crocker and D. G. Grier, "Methods of digital video microscopy for colloidal studies," *J. Colloid Interf. Sci.* **179**(1), 298-310 (1996).

88. O. Otto, C. Gutsche, F. Kremer and U. F. Keyser, "Optical tweezers with 2.5 khz bandwidth video detection for single-colloid electrophoresis," *Rev. Sci. Instrum.* **79**(2 Pt 1), 023710 (2008).

89. A. Van der Horst and N. R. Forde, "Power spectral analysis for optical trap stiffness calibration from high-speed camera position detection with limited bandwidth," *Opt. Express* **18**(8), 7670-7677 (2010).

90. R. Kubo, "The fluctuation-dissipation theorem,"*Rep. Prog. Phys.***29**(1), 255 (1966).

91. F. Merenda, G. Boer, J. Rohner, G. Delacrétaz and R.-P. Salathé, "Escape trajectories of single-beam optically trapped micro-particles in a transverse fluid flow," *Opt. Express* **14**(4), 1685-1699 (2006).

92. S. Keen, J. Leach, G. Gibson and M. J. Padgett, "Comparison of a high-speed camera and a quadrant detector for measuring displacements in optical tweezers,"*J. Opt. A***9**(8), S264 (2007).

93. F. Czerwinski, A. C. Richardson and L. B. Oddershede, "Quantifying noise in optical tweezers by allan variance," *Opt. Express* **17**(15), 13255-13269 (2009).

94. M. W. Allersma, F. Gittes, M. J. deCastro, R. J. Stewart and C. F. Schmidt, "Two-dimensional tracking of ncd motility by back focal plane interferometry," *Biophys. J.* **74**(2 Pt 1), 1074-1085 (1998).

95. P. M. Hansen, I. M. Tolic-Nørrelykke, H. Flyvbjerg and K. Berg-Sørensen, "Tweezercalib 2.0: Faster version of matlab package for precise calibration of optical tweezers," *Comput. Phys. Commun.* **174**(6), 518-520 (2006).

96. P. M. Hansen, I. M. Tolic-Nørrelykke, H. Flyvbjerg and K. Berg-Sørensen, "Tweezercalib 2.1: Faster version of matlab package for precise calibration of optical tweezers," *Comput. Phys. Commun.* **175**(8), 572-573 (2006).

Chapter 2

Combined optical micromanipulation and interferometric topography (COMMIT)

Abstract. Optical tweezers has emerged as a prominent light-based tool for pico-Newton (pN) force microscopy in mechanobiological studies. However, the efficacy of optical tweezers is limited in applications where concurrent metrology of the nano-sized structure under interrogation is essential to the quantitative analysis of its mechanical properties and various mechanotransduction events. We have developed an all-optical platform delivering pN force resolution in parallel to ≈ 30 nm (or better) axial resolution in biological samples by combining optical tweezers with interferometric quantitative phase microscopy. These capabilities allow real-time micromanipulation and label-free measurement of sample's nanostructures and nanomechanical responses, opening avenues to a wide range of new research possibilities and applications in biology.

Keywords: Optical tweezers or optical manipulation; Interference microscopy; Instrumentation, measurement, and metrology.

2.1 Introduction

Optical tweezers (OTs) continue to remain a desired, and in many cases, the only non-destructive tool in biophysical studies that involve force measurements on the cellular, sub-cellular, and molecular scales.[97-100] Quantitative mechanobiological studies are relevant to understanding of cellular processes such as morphogenesis, differentiation,

cytokinesis, growth, and motility.[101] We and others have utilized OTs to study membrane-based transduction,[102, 103] and membrane-cytoskeleton interactions by extracting membrane nanotubes (tethers) from cells.[31, 104]

While OTs provides excellent resolution in force measurements, sub-diffraction morphological changes in the load-bearing elements are undetectable using conventional microscopy. Super-resolution microscopy (SRM) methods employing fluorescent labels are not favorable as they impose changes on the molecular structures of the specimen[105] that affect its mechanical behavior[106]. Similarly, scanning probe SRM techniques such as atomic force microscopy (AFM)[107], tip-enhanced near-field optical microscopy,[108] and the recent method of scanning optically trapped spheres for surface imaging[109] are not suitable for concurrent micromanipulation and wide-filed imaging of the sample. In addition to their poor temporal resolution for wide-field imaging, such techniques inherently disturb local force fields and may apply additional forces to the sample.

Although electron microscopy in fluids has been made possible,[110] its application to live samples is limited mainly due to radiation damage, and decreased resolution in imaging depth.[111] Low imaging contrast in addition to complex substrate, sample, and chamber preparations required to integrate electron microscopy with other microscopy modes further complicate its use in biological studies.

Interferometric quantitative phase microscopy (QPM) offers a method for SRM of transparent and semi-transparent objects in a non-invasive and label-free manner.[112] The sample's thickness, and the mismatch between its refractive index (RI) and that of the surrounding medium result in optical path-length delays that can be resolved at sub-

nanometer resolution using QPM. Wide-field SRM at video rates and the ease of integrating QPM methods with other investigative techniques (such as fluorescence microscopy) has led to a growing application of QPM to the functional and structural biological studies.[113, 114]

Here we report on a platform that for the first time combines stiffness-calibrated OTs with an interferometric QPM technique based on Zernike's phase contrast and Gabor's holography.[115] This combined optical micromanipulation and interferometric topography (COMMIT) platform allows simultaneous measurements of pN level forces with nm scale spatial resolution associated with the object under interrogation. Low coherence illumination and common-path interferometry allow for speckle-free imaging[115] at high phase stability.[116]

2.2 Methods

2.2.1 COMMIT platform

Figure2.1 shows a schematic of the COMMIT platform integrating OTs and interferometric QPM. We have previously reported the details of the OTs setup and stiffness calibration for optical micro manipulation and force microscopy.[117] Briefly, a Nd:YVO_4 laser beam (Prisma 1064-V, Coherent, Santa Clara, CA) was expanded and coupled into an inverted microscope (Ti-Eclipse, Nikon Inc., Melville, NY) to form the optical trap. A 100X oil immersion objective lens (N.A. 1.49, Apo-TIRF, Nikon) was used for simultaneous imaging and optical trapping. A piezoelectric stage with 1 nm precision in x, y, and z coordinates was used to control the relative position of samples

and the optical trap. Sulfate-modified polystyrene microspheres with a mean diameter of 4.2 μm (Molecular probes, Eugene, OR) were used as handles for pulling tethers, and optical probes for force measurements.

The sample was illuminated by a 100W halogen lamp through a condenser annulus. Light that passes through the sample unscattered (U_0) forms the image of the condenser annulus at the Fourier plane of the achromatic doublet (L_1). A reflective spatial light modulator (SLM) (Hamamatsu Corp., Bridgewater, NJ) was used to shift the phase of U_0 in four $\pi/2$ steps. The unscattered component interferes with the unmodulated scattered field (U_1) to form the sample's image on the detector at the focal plane of the second achromatic doublet (L_2).

An EM-CCD (C9100-13, Hamamatsu) captured the intensity maps of the sample (I_{1-4}) corresponding to the four phase modulations. CCD's exposure time was set to 30.5 ms. To accommodate full re-arrangement of the nematic liquid crystals in the SLM, field delays of 83 ms (SLM response time for a $\pi/2$ modulation) were used between the phase modulations. Twelve phase shifted images were acquired every second to yield quantitative phase resolved images at 3 fps. To obtain the phase delay map (φ), we first calculated the phase difference between U_0 andU_1 using the four intensity maps:

$$\Delta\varphi = \tan^{-1}\left[(I_1 - I_3)/(I_2 - I_4)\right] \tag{2.1}$$

The phase delay map was then calculated as:

$$\varphi = \tan^{-1}\left[\beta\sin(\Delta\varphi)/(1+\beta\cos(\Delta\varphi))\right] \tag{2.2}$$

where $\beta=|U_1|/|U_0|$. The calculated phase delay map is correlated with the sample's thickness along the propagation axis of the light (d_z), center wavelength of the illumination (λ=595 nm), and the local differences between the RIs of the sample and the surrounding medium (n_s and n_r, respectively):

$$\varphi = \frac{2\pi}{\lambda}(n_r - n_s)d_z \tag{2.3}$$

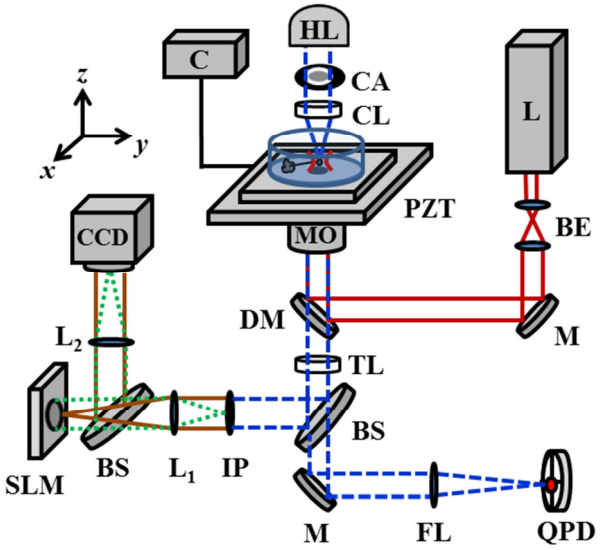

Fig. 2.1 Schematic of the COMMIT platform. HL: Halogen lamp. CA: Condenser annulus. CL: Condenser lens. C: PZT controller. MO: Microscope objective. L: Nd:YVO_4 laser. BE: Beam expander. M: Mirror. DM: Dichroic mirror. TL: Tube lens. BS: Beam splitter. FL: Focusing lens and IR filter. IP: Image plane and polarizer. L_1 and L_2: Achromatic doublets, f = 500 mm. SLM: Spatial light modulator.

We calibrated the stiffness of the optical trap against viscous drag forces since the trapped particle undergoes large displacements in our experiments.[117] Microspheres were trapped inside Modified Eagle Medium (MEM) at 37 °C, and a piezoelectric stage (Physik Instrumente, Waldbronn, Germany) was used to move the trapping medium against the optically trapped particle at various speeds. For the force calibration process,

microsphere's displacements from the center of the optical trap were monitored at 10 KHz using a QPD (Pacific Silicon Sensor, Westlake Village, CA) in imaging mode, delivering a 10 nm resolution. Viscous drag forces were plotted against microsphere displacements to calculate the OTs stiffness (see Appendix A for more details). Sub-pixel particle tracking[86] was used during cell experiments to calculate microsphere displacements in the CCD images at 10 nm spatial resolution.

2.2.2 Validation of interferometric QPM

A custom made microchip and polystyrene nanospheres of two different diameters were used to verify the validity of the topographical results. To fabricate the microchip, a microscope glass coverslip was spin coated with polymethylmethacrylate (PMMA) (MicroChem, Westborough, MA) at 4,000 rpm for 30 seconds. After spinning, the chip was transferred to a hot plate and heated to 180°C for 80 seconds. Arrays of patterns were then etched into the microchip using electron beam lithography (Leo SUPRA 55, Zeiss, Oberkochen, Germany). The resulting patterns have depths ranging between 150 to 190 nm. An area on the chip was selected and imaged using AFM (Smart SPM-1000, AIST-NT Inc., Novato, CA) for comparison with the QPM topography results of the same region.

In addition to using the custom made microchip, we validated our system's QPM measurements by imaging polystyrene nanospheres with manufacturer (Molecular Probes, Eugene, OR)-reported mean diameters ± standard deviation (SD) of 400 ± 17 nm and 630 ± 16 nm. The nanospheres were dispersed in water, transferred onto a microscope coverslip, and allowed to dry before imaging.

2.2.3 Cell culture and tether formation

We used the COMMIT platform to simultaneously form, image, and measure the dynamic forces associated with membrane tethers pulled from kidney (HEK-293) cells, as a model nano-structured system.HEK-293 cells were seeded onto glass-bottom petri dishes coated with Poly-L-Lysine 24 hours before the experiments. Cells were cultured at 37 °C and 5% CO_2 in a medium consisting of minimum essential medium (MEM) and 10% fetal bovine serum. Prior to pulling tethers, cells were washed with 1X phosphate buffer saline, and the culture medium was replaced by a mixture of MEM and 4.2 μm microspheres. A microsphere was optically trapped and brought into contact with the membrane of an adhered cell until a surface attachment between the microsphere and the cell membrane was confirmed. The cell was then moved away from the optically trapped particle at 1 μm/s using the piezoelectric stage, extruding a membrane tether.

2.3 Results and discussion

The AFM-based topography and QPM-resolved image of the custom made microchip are shown in Figs. 2.2a(i) and 2.2a(ii), respectively, and compared with each other in Fig. 2.2a(iii). While the lateral resolution of the quantitative phase image is diffraction limited, parallel to the direction of light propagation, QPM reported the size of the sub-diffraction structures within ± 7.2 nm of the corresponding features measured using AFM. The mean ± SD depth of the microchip features were measured as 179 ± 15 nm using AFM and 172 ± 16 nm using QPM. Figure2.2b shows the Polystyrene nanospheres resolved by QPM. Assuming $n_{\text{polystyrene microsphere}}$ =1.59, the QPM-resolved mean ± SD

nanosphere diameters of 425 ± 13 nm and 616 ± 16 nm are in good agreement with those reported by the manufacturer.

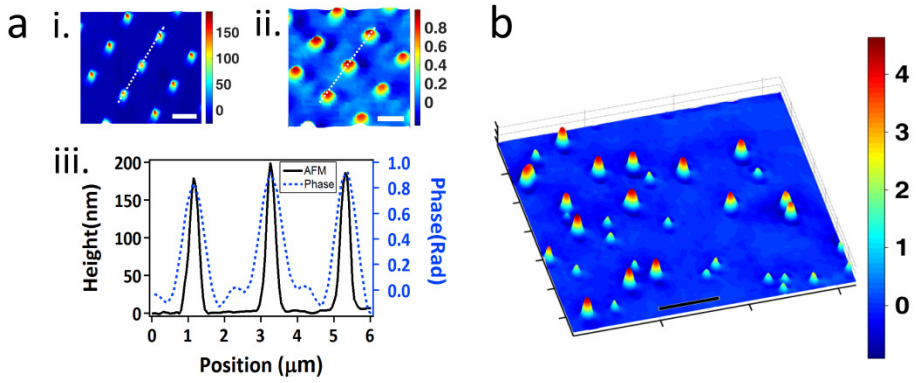

Fig. 2.2 (a): Comparison between topographical results of AFM and quantitative phase imaging for a custom made microchip. (i): Inverted AFM image of the custom made microchip; the color bar is in nanometers. (ii): Quantitative phase image of the region shown in (i); color bar is in radians. (iii): Overlapped cross sections of (i) and (ii) along the dotted lines. Scale bars in panels (i) and (ii) = 2 µm. (b): Pseudo-3D representation of a quantitative phase image of two sets of polystyrene nanospheres. Manufacturer-reported mean ± SD diameters of the nanospheres were 400 ± 17 nm and 630 ± 16 nm. Diameters measured using the QPM setup were 425 ± 13 nm and 616 ± 16 nm. Color bar is in radians. Scale bar = 5 µm.

Figure 2.3 shows the quantitative phase image of a tether extracted from a HEK-293 cell using the COMMIT platform. In the absence of experimental methods to verify the nanostructure of cell membrane tethers, mechanical models of tethers have been widely based on the tenet that lipid membrane nanotubes exhibit perfect cylindrical shapes at equilibrium.[118, 119] For the first time, these label-free super resolution images reveal curvatures and diameter changes along the tether axis that are well below the diffraction limit. The curved (catenoid) shape of the tether contour is in agreement with the predictions of recent multi-scale molecular models of bilayer nanotubes.[120]

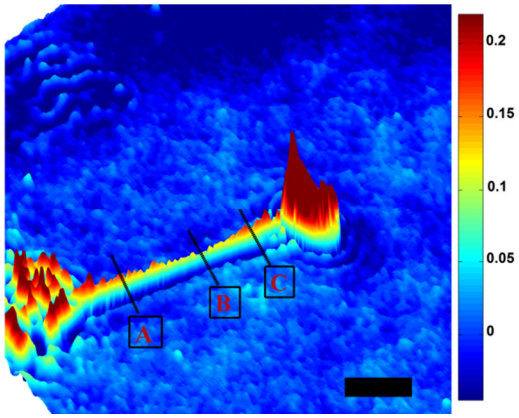

Fig. 2.3 Pseudo-3D representation of the quantitative phase image of a tether extracted from a HEK-293 cell using the COMMIT platform. Thinning along the tether axis results in a catenoid-like contour. Tether diameters at the A, B, and C boxed sections are measured as 456 nm, 253 nm, and 497 nm, respectively. Color bar is in radians. Scale bar = 5 μm.

Using the COMMIT platform, we were also able to study the dynamic process of membrane nanotube formation. Figure 2.4 and Movie 1 (see Appendix B) show an illustrative example of concurrent optical micromanipulation, force microscopy, and structural metrology during a membrane tether experiment. An optically trapped 4.2 μm microsphere was used to form a tether by detaching the cell membrane from the underlying cytoskeleton (Fig. 2.4a). Following the detachment of a patch of membrane from the cytoskeleton, tether reaction force decreases during the elongation interval (Fig. 2.4b). Membrane tether ruptures in reaction to the increased pulling force (Fig. 2.4c). Subsequently, lipid bilayer re-assembles at the either ruptured end of the tether resulting in a brief reversal of the reaction force direction (Fig. 2.4d).

The maximum imaging resolution of the QPM method depends on the RI difference between those of the sample (n_s) and the surrounding medium (n_{media}) (Eq. 2.3), and is ultimately limited by the compound temporal phase noise of the system (5 mrad in our

current setup). The QPM method employed in this study has been previously shown to produce topographical results from graphene structures at sub-nanometer accuracy.[121] In cellular applications, where low RI differences are involved (n_{cell} reported in the range of 1.354[122] to 1.8[123] and n_{media}=1.337), the topography resolution of our platform ranges from 11 to 28 nm.

Force-calibrated optical micromanipulation in conjugation with video rate QPM facilitates dynamic measurement of the transient nano-scale mechanical properties of cells and intracellular organelles, by bridging nanomechanical measurements with real-time nano-structural information. Cellular mechanical properties are regarded as highly sensitive markers of disease.[124, 125] QPM conjoined with machine learning algorithms is also being investigated as a marker-free diagnostic tool in histopathology.[114] Therefore, COMMIT can potentially improve the reliability of the histological findings by combining both of these analytical capabilities in one platform. In mechanobiology studies, COMMIT can provide an unprecedented capability for simultaneous induction of precise mechanical stimuli along with quantitative analysis of the mechanical responses, and *in-vivo* measurement of the resulting sub-diffraction cell shape changes and organelle deformations.[126]

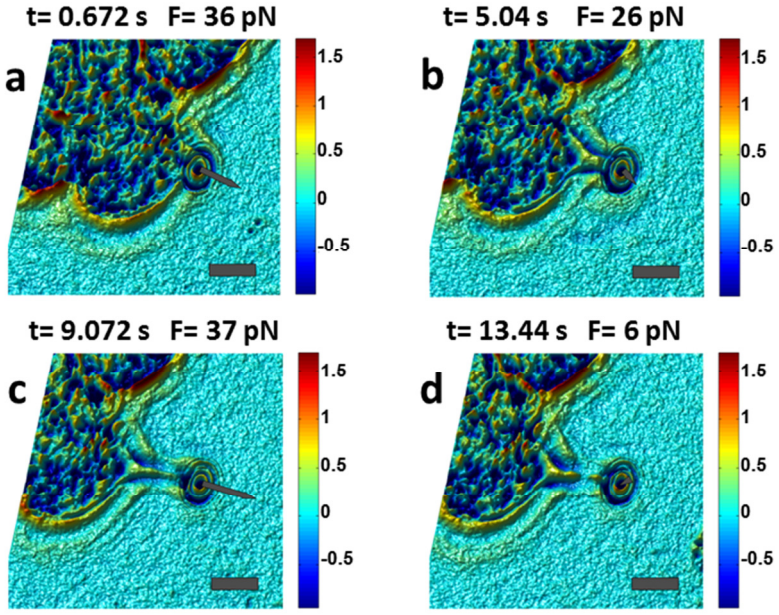

Fig. 2.4 Dynamic quantitative measurement of membrane tether structure and reaction force during various time intervals (see Movie 1).(a): Tether formation interval. (b): Tether elongation interval. Tether reaction force decreases following the formation interval. (c): Increased pulling force results in tether rupture. (d): Lipid membrane reassembles on both ends of the ruptured tether and the direction of the reaction force is momentarily reversed (recoil). Increased diameters at both ends are resolved as a result of membrane folding. The arrows represent the magnitude and direction of tether reaction force. Color bars are in radians. Scale bars = 10 μm.

2.4 Conclusions

We have provided the first demonstration of an experimental platform combining force calibrated OTs and QPM for concurrent optical micromanipulation at nanometer scale, pN force microscopy, and wide-field label-free non-invasive super resolution metrology of the sample. Our experimental platform enables new discoveries in a wide range of mechanobiological studies.

2.5 References

31. N. Khatibzadeh, A. A. Spector, W. E. Brownell and B. Anvari, "Effects of plasma membrane cholesterol level and cytoskeleton f-actin on cell protrusion mechanics," *PLoS ONE* **8**(2), e57147 (2013).

86. R. Parthasarathy, "Rapid, accurate particle tracking by calculation of radial symmetry centers," *Nat. Meth.* **9**(7), 724-726 (2012).

97. A. Ashkin, K. Schutze, J. M. Dziedzic, U. Euteneuer and M. Schliwa, "Force generation of organelle transport measured in vivo by an infrared laser trap," *Nature* **348**(6299), 346-348 (1990).

98. B. H. Blehm and P. R. Selvin, "Single-molecule fluorescence and in vivo optical traps: How multiple dyneins and kinesins interact," *Chem. Rev.* **114**(6), 3335-3352 (2014).

99. F. M. Fazal and S. M. Block, "Optical tweezers study life under tension," *Nature Photonics* **5**(6), 318-321 (2011).

100. M. J. Siedlik, V. D. Varner and C. M. Nelson, "Pushing, pulling, and squeezing our way to understanding mechanotransduction," *Methods*, (2015).

101. T. Iskratsch, H. Wolfenson and M. P. Sheetz, "Appreciating force and shape - the rise of mechanotransduction in cell biology," *Nature Reviews Molecular Cell Biology* **15**(12), 825-833 (2014).

102. W. E. Brownell, F. Qian and B. Anvari, "Cell membrane tethers generate mechanical force in response to electrical stimulation," *Biophys. J.* **99**(3), 845-852 (2010).

103. N. C. Gauthier, M. A. Fardin, P. Roca-Cusachs and M. P. Sheetz, "Temporary increase in plasma membrane tension coordinates the activation of exocytosis and contraction during cell spreading," *Proc. Natl. Acad. Sci. U.S.A.* **108**(35), 14467-14472 (2011).

104. D. Raucher, T. Stauffer, W. Chen, K. Shen, S. Guo, J. D. York, M. P. Sheetz and T. Meyer, "Phosphatidylinositol 4,5-bisphosphate functions as a second messenger that regulates cytoskeleton-plasma membrane adhesion," *Cell* **100**(2), 221-228 (2000).

105. H. Bouvrais, T. Pott, L. A. Bagatolli, J. H. Ipsen and P. Méléard, "Impact of membrane-anchored fluorescent probes on the mechanical properties of lipid bilayers," *BBA-Biomembranes* **1798**(7), 1333-1337 (2010).

106. V. Lulevich, Y. P. Shih, S. H. Lo and G. Y. Liu, "Cell tracing dyes significantly change single cell mechanics," *J. Phys. Chem. B* **113**(18), 6511-6519 (2009).

107. D. J. Müller and Y. F. Dufrêne, "Atomic force microscopy as a multifunctional molecular toolbox in nanobiotechnology," *Nat. Nano.* **3**(5), 261-269 (2008).

108. N. Mauser and A. Hartschuh, "Tip-enhanced near-field optical microscopy," *Chem. Soc. Rev.* **43**(4), 1248-1262 (2014).

109. L. Friedrich and A. Rohrbach, "Surface imaging beyond the diffraction limit with optically trapped spheres," *Nature Nanotechnology*, (2015).

110. S. Thiberge, A. Nechushtan, D. Sprinzak, O. Gileadi, V. Behar, O. Zik, Y. Chowers, S. Michaeli, J. Schlessinger and E. Moses, "Scanning electron microscopy of cells and tissues under fully hydrated conditions," *Proc. Natl. Acad. Sci. U.S.A.* **101**(10), 3346-3351 (2004).

111. N. de Jonge and F. M. Ross, "Electron microscopy of specimens in liquid," *Nat. Nano.* **6**(11), 695-704 (2011).

112. B. Kemper and G. von Bally, "Digital holographic microscopy for live cell applications and technical inspection," *Appl. Opt.* **47**(4), A52-A61 (2008).

113. G. Popescu, L. P. Deflores, J. C. Vaughan, K. Badizadegan, H. Iwai, R. R. Dasari and M. S. Feld, "Fourier phase microscopy for investigation of biological structures and dynamics," *Opt. Lett.* **29**(21), 2503-2505 (2004).

114. S. Sridharan, V. Macias, K. Tangella, A. Kajdacsy-Balla and G. Popescu, "Prediction of prostate cancer recurrence using quantitative phase imaging," *Sci. Rep.* **5**, 9976 (2015).

115. Z. Wang, L. Millet, M. Mir, H. Ding, S. Unarunotai, J. Rogers, M. U. Gillette and G. Popescu, "Spatial light interference microscopy (slim)," *Opt. Express* **19**(2), 1016-1026 (2011).

116. B. Kemper, A. Vollmer, C. E. Rommel, J. Schnekenburger and G. v. Bally, "Simplified approach for quantitative digital holographic phase contrast imaging of living cells," *J. Biomed. Opt.* **16**(2), 026014 (2011).

117. M. Sarshar, W. T. Wong and B. Anvari, "Comparative study of methods to calibrate the stiffness of a single-beam gradient-force optical tweezers over various laser trapping powers," *J. Biomed. Opt.* **19**(11), 115001 (2014).

118. R. E. Waugh and R. M. Hochmuth, "Mechanical equilibrium of thick, hollow, liquid membrane cylinders," *Biophys. J.* **52**(3), 391-400 (1987).

119. F. Brochard-Wyart, N. Borghi, D. Cuvelier and P. Nassoy, "Hydrodynamic narrowing of tubes extruded from cells," *Proc. Natl. Acad. Sci. U.S.A.* **103**(20), 7660-7663 (2006).

120. S. Baoukina, S. J. Marrink and D. P. Tieleman, "Molecular structure of membrane tethers," *Biophys. J.* **102**(8), 1866-1871 (2012).

121. Z. Wang, I. S. Chun, X. Li, Z.-Y. Ong, E. Pop, L. Millet, M. Gillette and G. Popescu, "Topography and refractometry of nanostructures using spatial light interference microscopy," *Opt. Lett.* **35**(2), 208-210 (2010).

122. C. L. Curl, C. J. Bellair, T. Harris, B. E. Allman, P. J. Harris, A. G. Stewart, A. Roberts, K. A. Nugent and L. M. D. Delbridge, "Refractive index measurement in viable cells using quantitative phase-amplitude microscopy and confocal microscopy," *Cytometry A* **65**(1), 88-92 (2005).

123. S. Przibilla, S. Dartmann, A. Vollmer, S. Ketelhut, B. Greve, G. von Bally and B. Kemper, "Sensing dynamic cytoplasm refractive index changes of adherent cells with quantitative phase microscopy using incorporated microspheres as optical probes," *J. Biomed. Opt.* **17**(9), 097001 (2012).

124. S. E. Cross, Y. S. Jin, J. Rao and J. K. Gimzewski, "Nanomechanical analysis of cells from cancer patients," *Nat. Nano.* **2**(12), 780-783 (2007).

125. J. Guck, S. Schinkinger, B. Lincoln, F. Wottawah, S. Ebert, M. Romeyke, D. Lenz, H. M. Erickson, R. Ananthakrishnan, D. Mitchell, J. Kas, S. Ulvick and C. Bilby, "Optical deformability as an inherent cell marker for testing malignant transformation and metastatic competence," *Biophys. J.* **88**(5), 3689-3698 (2005).

126. J. D. Szafranski, A. J. Grodzinsky, E. Burger, V. Gaschen, H.-H. Hung and E. B. Hunziker, "Chondrocyte mechanotransduction: Effects of compression on deformation of intracellular organelles and relevance to cellular biosynthesis," *Osteoarthr. Cartil.* **12**(12), 937-946 (2004).

Chapter 3

Dynamics of membrane tethers extruded from HEK293 cells with intact and disrupted cytoskeleton: a COMMIT Study.

Abstract. Plasma membrane tethers are involved in various cellular functions such as motility, cell communications, and transmission of pathogens. Tether extrusion from cells is a widely practiced experimental technique providing quantitative information on membrane mechanical properties and membrane-cytoskeleton interactions. In the absence of techniques for concurrent force microscopy and quantification of membrane nanostructures, tether studies have primarily focused on analyzing the tether reaction forces. We used the COMMIT platform for simultaneous extrusion, force microscopy, and super resolution imaging of membrane tethers from cytoskeleton intact and disrupted HEK239 cells. We were able to observe the force-active sub-resolution heterogeneities in tether diameter along its length. We report on observation of cell's active maintenance of low membrane curvature at the base of the tether to facilitate tether tension relaxation by the Marangoni flow. We also show that the cells are capable of inducing functional shape changes in the tether even in the absence of a functional cytoskeleton.

3.1 Introduction

The plasma membrane is a key player in vital cellular functions such as motility, growth, and mitosis. Membrane studies by means of forming membrane nanotubes, also called tethers, have given valuable insight into mechanics of plasma membranes, membrane-cytoskeleton interactions, and mechanotransduction.[127-129] Naturally occurring membrane tethers function in adhesion,[130, 131] cell-cell communication,[132-135] and transmission of pathogens.[134, 135]Studying membrane tethers allows for quantification of membrane properties including bending modulus, viscosity, and tension, which are mediators and drivers of physiological functions like trafficking, cell motility, and cell division.[128, 136, 137]

Membrane tethers are usually extruded through micropipette aspiration, atomic force microscopy, magnetic tweezers, or optical tweezers,[128, 138-140] with the latter delivering the highest force resolution.[27, 141]As changes in tether diameter and profile often fall below the diffraction limit, conventional microscopy techniques cannot be used to study membrane tether geometry. In the absence of label-free non-invasive microscopy approaches to quantitatively study membrane nanostructures, tether studies mainly focus on the dynamic measurement and analysis of tether reaction forces under various mechanical and chemical manipulation regimes.[137, 138, 142]

By assuming simple cylindrical shapes for tethers,[118, 119, 127, 140] the dynamic tether profile changes that accompany the aforementioned forces have not been extensively studied. We recently developed and reported on a COMMIT (Combined Optical Micro-Manipulation and Interferometric Topography) platform that allows for concurrent

optical force microscopy and quantitative imaging of cellular structures at nanometer resolution. In this study, we have utilized COMMIT to study the dynamics of normal and cytoskeleton-disrupted human embryonic kidney (HEK293) cell membrane tethers. We simultaneously formed membrane tethers from normal and cytoskeleton-disrupted cell and measured tether structure and reaction forces. We compare the results and discuss the cellular behavior in maintaining the membrane tether under the two cases in the following.

3.2Methods

3.2.1 COMMIT platform

3.2.1.1 Optical micromanipulation and force microscopy

The setup, calibration, and validation of the COMMIT platform used to form and study the HEK293 cell membrane tethers is detailed in 2.2.1. In brief, a Nd:YVO_4 laser (Prisma 1064-V, Coherent, Santa Clara, CA) and a 100X oil immersion objective lens (N.A. 1.49, Apo-TIRF, Nikon Inc., Melville, NY) were used to form the laser tweezers for optical manipulation and force microscopy. The expanded trapping laser beam was coupled into the microscope objective (Ti-Eclipse, Nikon) by a dichroic mirror (680dcspxr-laser, Chroma Technology Corp, Bellow Falls, VT) with 90% transmittance at 470-650 nm, allowing for simultaneous optical trapping and imaging of the sample.

The spatial control of the relative position of the trap and HEK293 cells was achieved using a piezoelectric stage with 1 nm precision in x, y, and z coordinates (Physik Instrumente, Waldbronn, Germany). Stiffness of the optical trap was calibrated against

known viscous drag forces as described in 1.2.3.1, with spring constant k= 320 pN.µm^{-1}for 500 mW of laser delivered at the specimen plane.

3.2.1.2 Quantitative phase imaging (QPI) at improved rate

COMMIT illuminates the sample through a condenser annulus to perform QPI. A 4*f* configuration is used to spatially separate and later recombine the unscattered (U_0) and scattered (U_1) light fields that pass through the sample (Fig. 2.1). At the Fourier plane of the first achromatic doublet (L_1), U_0forms the image of the condenser annulus through which the sample is illuminated. A reflective spatial light modulator (SLM) (LCOS-SLM X10468, Hamamatsu Corp., Bridgewater, NJ) was used to overlay a phase shift mask with the image of the condenser annulus, creating four $\pi/2$phase modulated states of the reflected U_0 field ($M_{1\text{-}4}$) with respect to the reflected U_1. The two fields interfere at the focal plane of the second achromatic doublet (L_2) to form four intensity maps of the sample image ($I_{1\text{-}4}$) corresponding to the four phase modulations.

The intensity maps $I_{1\text{-}4}$were recorded using an EM-CCD camera (C9100-13, Hamamatsu) at 35.8 fps with the exposure time of 28 ms. Knowing the mismatch between the refractive indices of the sample and the surrounding medium (n_s and n_r, respectively), the optical thickness of the sample along the propagation axis of the light (d_z) can be calculated from the phase delay maps of the sample via Eq. (2.1-2.3). The QPI rate in this scheme is limited by the response delay (transitioning time when switching between two separate phase modulations) of the SLM. A survey of the currently commercially available SLMs reveal that regardless of their digital refresh rate, most2D SLMs providing full 2π phase modulation over the visible wavelengths have minimum

phase response delays of tens of milliseconds. For example, the response times of our SLM for different switching possibilities between the $M_{1\text{-}4}$ states range from 25 ms to 100 ms.

For this study we improved the previously reported 3 fps QPI rate of the COMMIT platform by changing the pattern of phase modulations. A mirrored pattern was used to decrease modulations required for resolving two QPIs from 8 to 6 (Fig 3.1a). Additionally, the arrangement of the subsequently modulated states was optimized to minimize the accumulative response delay within each repeating phase modulation cycle. A 30 ms delay between the modulations was added to the calculated response delay of each modulation to ensure that at least one image of the modulated state after the phase transition period is collected. Given the unequal response delays for each modulation and an independent image acquisition platform, time intervals between the four recorded modulated states needed to resolve one QPI may vary. A MATLAB™ (The MathWorks, Natick, MA) routine was developed to analyze the intensity maps acquired by the CCD and separate $M_{1\text{-}4}$ states for subsequent phase calculations (see Appendix C). Analysis of the timestamps of the resolved QPIs reveals mean ± standard deviation intervals of 0.23±0.05 s between the QPI frames, suggestive of a 45% improvement over the last reported QPI acquisition rate.

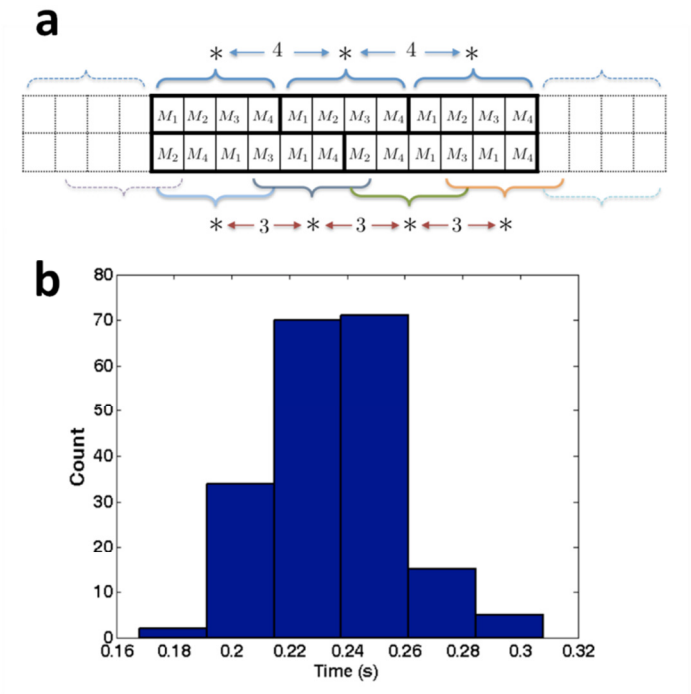

Fig. 3.1 Quantitative phase microscopy image acquisition rate improvement. (a) A change from the classic four $\pi/2$modulations (top line) reduces the effective number of phase modulations per resolved QPI from 4 to 3 (bottom line). (b) Time intervals between QPI results (mean±std = 0.23±0.05 s)corresponding to 4.3 fps.

3.2.2 Cell culture and cytoskeleton disruption

HEK293 cells were seeded onto glass-bottom poly-d-lysine coated petri dishes in a medium made of minimum essential medium (MEM), 10% fetal bovine serum, and 1 % penicillin. Cells were cultured at 37 °C and 5% CO2 for 36 hours prior to the experiments. To disrupt cell cytoskeletons, we incubated cells for 10 minutes with Latrunculin A (EDM Millipore, Temecula, CA) which prevents polymerization of actin monomers.[143] Latrunculin A was dissolved in DMSO and added to MEM to a final concentration of 0.24 µM while the DMSO in the final media remained under 0.05%. The Latrunculin A concentration and incubation time were chosen such that partial disruption

of cytoskeleton is achieved, preserving the ability of cells to linger themselves to the substrate through focal adhesion points during membrane tethering experiments.

Sulfate-modified polystyrene beads with 4.2 μm diameter (Molecular probes, Eugene, OR) were optically trapped in MEM and brought into contact with the cell membrane as handles for optical micromanipulation. After a surface adhesion was established between the trapped bead and cell membrane, a tether was formed by moving the cell away from the trapped bead at the speed of 1 μm/s by the piezo electric stage. We dynamically measured tether reaction forces and axial profiles under normal and cytoskeleton disrupted states, with the results presented in section 3.3.

3.3 Results

3.3.1 Tether dynamics of cytoskeleton-intact HEK293 cells

Figure 3.2 shows the time sequence of reaction forces and diameters of a tether formed from a cytoskeleton-intact HEK293 cell during 15 s of tether elongation followed by 45 s of quantitative observation of tether behavior post elongation. Figure 3.2a shows the cross section of the tether along its axis versus time, with time plots of tether reaction force and tether mean diameter along its axis presented in Fig 3.2b.

Tether reaction force remains high (> 200 pN) during the elongation interval with the highest values reached at the end of the elongation (260 pN at 15.6 s, marked A^* on Fig. 3.2a). Tether diameter changes in this interval with the highest values measured when the bead and cell are less than 8 μm apart (1100 nm). Following this point, tether mean diameter decays (tether thins) with a time constant of about 3 s to 850 nm, concurrent

with a decrease in the reaction force (Fig. 3.2, 8-11 s). After the tether mean diameter reaches a plateau, tether reaction forces start to grow with the tether length (Fig 3.2, 11-15 s). The tether profile in this period is smooth and uniform along the length of the tether with smaller diameters towards the bead and increasing diameters at the base of the tether near the cell body.

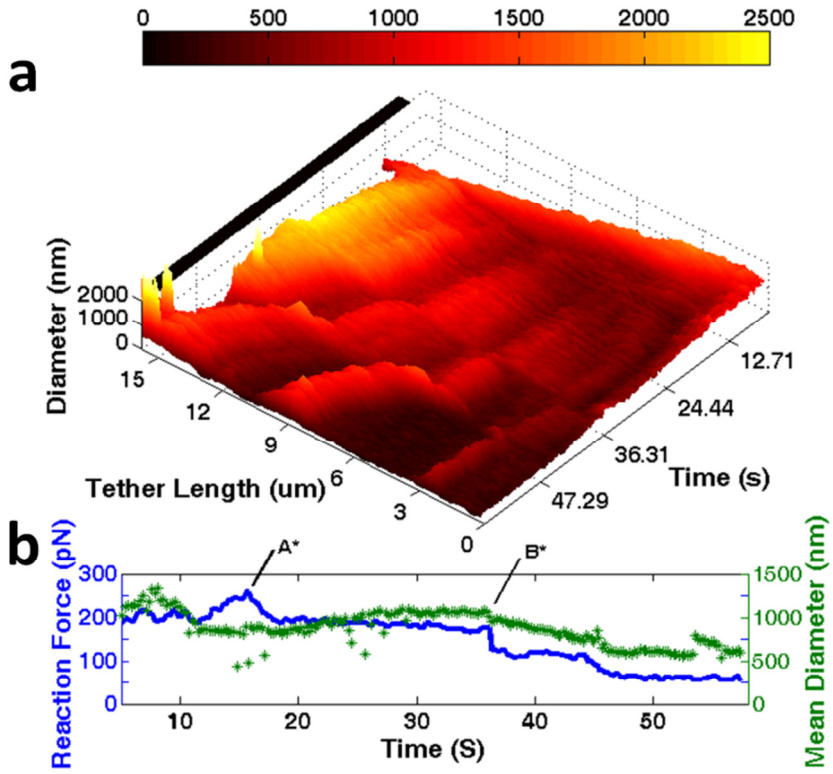

Fig. 3.2 Time sequence of reaction forces and diameters of a tether formed from a HEK293 cell with intact cytoskeleton. (a) Cross section of the tether along its axis versus time. Color bar is in nanometers. (b) Tether reaction force and mean diameter as a function of time. A^*: end of tether elongation. B^*: cell wall retraction at the base of the tether (see Fig. 3.3).

After tether elongation stops, the tether force decays with a time constant of 7.7 s reaching a value of about 200 pN, holding the tensing through a slow linear decrease to

170 pN while the mean diameter of tether gradually increases. Tether contour along its axis starts to transitions away from the smooth regime and develops regions of higher diameter along the axis, with higher diameters maintained at the base of the tether. At t=35 s (marked B* on Fig 3.2b), a sudden drop follows a local peak in tether reaction force (from 180 pN to about 115 pN), followed by a gradual decrease in tether mean diameter at this constant force (Fig 3.2, 36-44 s). A third decay in tether reaction force with a time constant of 16.9 s is seen as the tether thins on both ends while regions of much higher diameter are formed along the tether axis, maintaining an almost constant mean tether diameter in this interval. Figure 3.3 and Movie 2 (see Appendix B) show that concurrent with these events, cell begins a process of retracting its walls at the base of the tether and reshaping itself (Fig 3.2, 35-53 s).

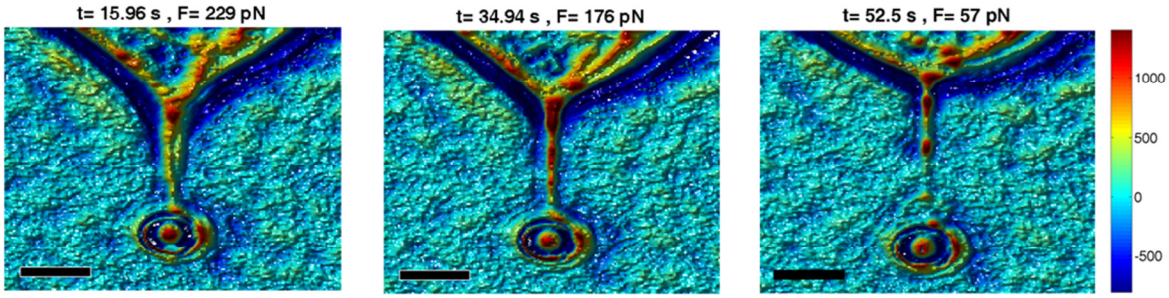

Fig. 3.3 Time sequence of tether profile, reaction force, and cell shapeat the base of the membrane tether formed from a HEK293 cell with intact cytoskeleton. t= 15-35 s: Cell slowly contracts at the base of the tether but tether base holds constant shape for the most part while tether diameter gradually increases. t= 35-52 s: Increase in wall retraction results in a local peak in tether reaction force, followed by a drop in reaction force and fast reshaping of the cell at tether base. Tether mean diameter decreases, and tether profile becomes heterogeneous (also see: Movie 2). F is the tether reaction force. Scale bar = 4 μm. Color bar is in nanometers.

3.3.2 Tether dynamics of cytoskeleton-disrupted HEK293 cells

Figure 3.4 shows the time sequence of reaction forces and diameters of a tether formed from a cytoskeleton-disrupted HEK293 cell during 14 s of tether elongation followed by 30 s of quantitative observation of tether behavior post elongation. Figure 3.4a shows the cross section of the tether along its axis versus time, with time plots of tether reaction force and tether mean diameter along its axis presented in Fig 3.4b.

The tether is extruded at low force (15 pN) which remains at the same level through the tether elongation interval (at 15 s, marked A^* on Fig. 3.4b). The tether is extruded at an initial diameter of 1900 nm. Mean diameter of the tether drops linearly independent of the elongation regime to its equilibrium value of 500 nm. Contrary to the cytoskeleton-intact case where the tether profile had smaller diameters towards the bead and increased diameters near the cell, here tether diameters along the axis range from 1000 nm adjacent to the bead to 250 nm towards the cell body.

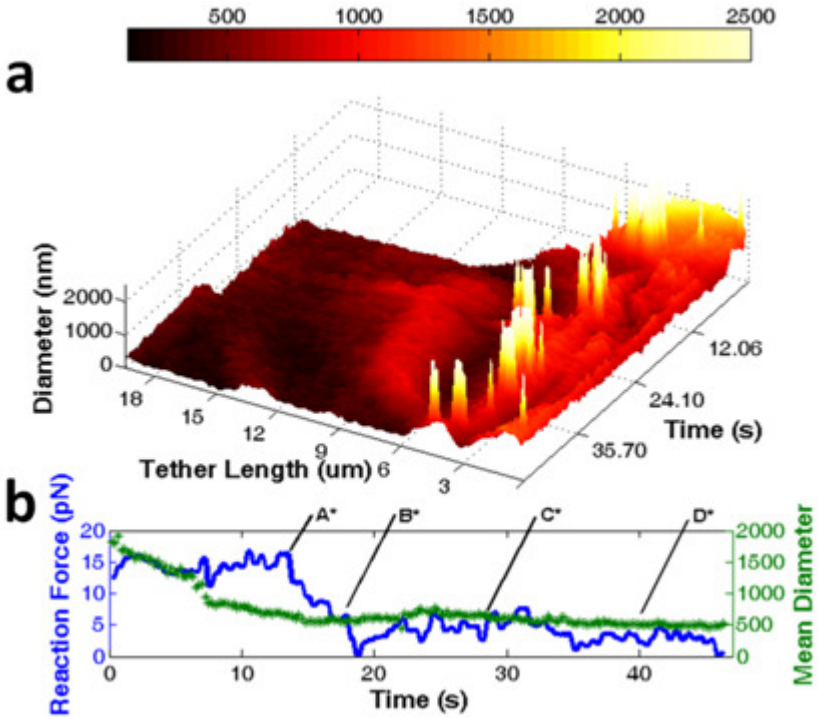

Fig. 3.4 Time sequence of reaction forces and diameters of a tether formed from a HEK293 cell with disrupted cytoskeleton. (a) Cross section of the tether along its axis versus time. Color bar is in nanometers. (b) Tether reaction force and mean diameter as a function of time. A^*: end of tether elongation. B^*, C^*, and D^*: cell wall retraction at the base of the tether.

Tether reaction force drops to 5 pN as the tether mean diameter drops to its mean equilibrium value (Fig. 3.4, 14-17 s). The cell wall is retracted at the tether extraction site at the times marked B^*, C^*, and D^*on Fig. 3.4b, producing negligible changes in the magnitudes of tether reaction force or tether mean diameter. However, the wall retractions are followed by changes in the tether contour and the locations of regions with higher diameters along the tether axis.

3.4 Discussion

The tension in the tether membrane (σ_t) is the sum of cell membrane tension (σ_c) and the work required for tether extrusion (W_e, the total work of changing membrane curvatures, linker detachments, and rearrangement of molecules)[119]. Tether diameter is related to the tension in the tether:[144]

$$d_t/2 = \sqrt{\frac{M_B}{2\sigma_t}} \tag{3.1}$$

where M_B is the effective bending modulus of the membrane. The higher tether diameters at the beginning of tether extrusion in the cytoskeleton-disrupted case are due to the lower tension in the cell membrane and lower extrusion work in the absence of an intact cytoskeleton. The smaller extrusion diameter of the tether in the cytoskeleton-intact case is suggestive of the effect of cytoskeleton in generating and maintaining tension in the membranes of both the cell and the tether.

Following tether extrusion and introduction of a tension difference between cell and tether membranes, two opposite membrane flows begin affecting the tether diameter: a slow Marangoni flow of membrane towards the area with higher tension to alleviate the lower membrane density; and a fast Poiseuille flow as a result of Laplace pressures towards the area with lower tension.[145] The narrowing of the tether along its axis that immediately follows the separation of bead from the cell body in both cases can be described by the Poiseuille flow. In the cytoskeleton-intact case, QPI-resolved tether contours suggest that this flow depletes tether from its excess membrane in this interval, resulting in the growth-dependent increase in the tether reaction force until the end of

elongation. Upon ending of the elongation interval, tether force relaxes to its rate-invariant magnitude with a time constant of 7.7 s, which is in agreement with previously reported data for similar cases.[30]

The slow effects of Marangoni flow are seen after the decay of the tether reaction force. The gradual increase in the tether mean diameter and decrease in the reaction force are indicative of decreased tether tension as a result of Marangoni flow. This hypothesis is supported by the QPI results showing the onset of membrane crumpling along the tether for establishing local mechanical equilibrium. Datar et al.[138] recently proposed a model in which the sharp membrane curvature at the base of the tether acts as a barrier between the two membrane states with higher and lower density, impeding the Marangoni flow. QPI-resolved profiles of the tether from the cytoskeleton-intact cell show a high tether diameter maintained adjacent to the cell body through this relaxation period. This tether contour effectively reduces the sharp curvatures that would otherwise inhibit tether tension relaxation and the subsequent tether diameter increase. Our results provide the first experimental evidence of cell's selective behavior in facilitating Morongoni flow for adjusting the tension in its tether, by maintaining a decreased membrane curvature at the tether base.

The gradual relaxation of the tension in the tether extracted from cytoskeleton-intact cell is accompanied by an increase in its diameter initiated at the base of the tether and propagating along its axis (Fig. 3.3). While tether reaction force does not show significant changes in this period, analysis of the QPI results shows a clear intrusion of cytoplasmic matter into the tether. The sudden drop in tether reaction force seen at point B^* in Fig.

3.2b is characteristic of breakage of cytoskeletal filaments under tensile stress. While tether mean diameter shows small changes following this drop in force, QPI images reveal substantial changes in tether profile. Tether diameter drops at both ends, while tether contents accumulate in regions of higher diameter formed along the axis of the tether. The smaller radius of these crumbles compared to that of the cell indicates that Laplace pressures should move tether contents towards the cell body. However, tether reaction force and the location of the crumbles along the tether remained the same for the next 8 s, suggestive of local adhesions between the tether membrane and its cytoplasmic content. During this time, the membrane curvature at the base of the tether changed as the cell begins to retract its wall.

Last force relaxation of the tether formed from the cytoskeleton-intact cell was initiated by a local deformation at the base of the tether. As evidenced by the QPI results, this decay is accompanied by a shift of the tether contents towards the cell body (Movie 2 and Fig. 3.2a, 44-53 s). Local deformations at the base of the tether gave rise to tether profile changes resembling a peristaltic motion although mean tether diameter does not reflect these changes as multiple foci of higher diameter moved along the tether. By the end of this interval, tether reaction force relaxes to its equilibrium value of about 40 pN and tether mean diameter decreases to 500 nm.

In the cytoskeleton-disrupted case, the low and constant reaction force during the elongation interval is evidence of free flow of membrane into the tether from the unbound membrane reservoir.[146] QPI reveals that in the absence of a significant membrane tension gradient at the beginning of tether extrusion, membrane moves towards both ends of the

tether as a result of the Poiseuille flow. This effect leads to tether membrane accumulation at the bead attachment site, contrary to the tether extruded from a cytoskeleton-intact cell. As the tether is elongated without the mediating role of cytoskeleton in regulating membrane tensions, tether maintains its highest diameter at the bead site while Laplace pressures keep the diameter of the tether along its body at the equilibrium value (280-350 nm).

In the cytoskeleton-disrupted case, tether reaction forces decrease to almost zero after elongation stops, as the membrane continues to flow into the tether maintaining its total tension homogeneous with the cell body. At this stage with reaction forces fluctuating <6 pN and no functional evidence of cytoskeletal involvement, the cell wall is retracted at the tether extraction site at time intervals of ~10 s (points B^*, C^*, and D^* on Fig. 3.4b). Negligible effect from these attempts is detectable in time profiles of tether reaction force and mean diameter. However, similar to the cytoskeleton-intact case, QPI revealed peristaltic-like changes along the tether axis following local curvature changes generated at the base of the tether (Movie 3, see Appendix B). Even at the absence of an active cytoskeleton, low energy local modulation in lipid density or diameter at the base of the tether allows the cell to use membrane's viscoelastic properties to introduce a shape change in the tether. This shape change can in turn invoke a secondary flow (such as Poiseuille flow), resulting in the transfer of matter along the tether at little energetic cost to the cell.

Cell uses the membrane's tendency to keep a homogeneous total tension for sensing its environment far from the cell body without needing to rely on the slow and energy

intensive rearrangement of its cytoskeleton. Similarly, by controlling the membrane tension, cell can apply forces (or send mechanically-mediated signals) where its cytoskeleton is not present. Cellular functions from motility and spreading[103, 147] to the polymerization rate of cytoskeletal filaments in tethers[148] are regulated via membrane tension. We reviewed an example of how the cell uses its cytoskeleton to control the tension in its membrane, regulating the shape of its tether and promoting the intrusion of cytoskeleton inside the tether. Cells make and break multiple tethers while moving and communicating with their environment. They maintain both cytoskeleton-permeated and cytoskeleton-devoid tethers for reasons such as controlling their rate of motility and contact area.[131, 149] In addition to discussing the role of cytoskeleton in membrane tension maintenance, we also discussed the ability of cell to induce shape changes in its protrusions devoid of functioning cytoskeleton.

3.5 Conclusion

Cellular tethers are complex nanostructures exhibiting active behaviors different than those of bilayer tethers extruded from vesicles. As such, negligence to quantify the nanostructure of the tether by assuming it as a cylindrical structure with a mean diameter can lead to misinterpretation of the experimental data. We used COMMIT to study the dynamics of membrane tethers extruded from HEK293 cells with intact and disrupted cytoskeletons. Combined optical force microscopy and super resolution QPI allowed us to dynamically quantify both nanomechanical forces and nanostructures of the membrane tethers during the experiments. We made the first observation of cell's active

maintenance of low membrane curvature at the base of the tether to facilitate tension relaxation by the Marangoni flow. Using QPI we were also able to show that the cell can sense tensions and induce functional shape changes in the tether even in the absence of cytoskeleton. The experimental data made accessible through COMMIT can be used for dynamic mechanical, structural, and functional modeling to add new insights into every biomechanical phenomenon involving sub-diffraction shape changes.

3.6 References

27. K. C. Neuman and A. Nagy, "Single-molecule force spectroscopy: Optical tweezers, magnetic tweezers and atomic force microscopy," *Nat. Methods* **5**(6), 491-505 (2008).

30. N. Khatibzadeh, S. Gupta, B. Farrell, W. E. Brownell and B. Anvari, "Effects of cholesterol on nano-mechanical properties of the living cell plasma membrane," *Soft Matter* **8**(32), 8350-8360 (2012).

103. N. C. Gauthier, M. A. Fardin, P. Roca-Cusachs and M. P. Sheetz, "Temporary increase in plasma membrane tension coordinates the activation of exocytosis and contraction during cell spreading," *Proc. Natl. Acad. Sci. U.S.A.* **108**(35), 14467-14472 (2011).

118. R. E. Waugh and R. M. Hochmuth, "Mechanical equilibrium of thick, hollow, liquid membrane cylinders," *Biophys. J.* **52**(3), 391-400 (1987).

119. F. Brochard-Wyart, N. Borghi, D. Cuvelier and P. Nassoy, "Hydrodynamic narrowing of tubes extruded from cells," *Proc. Natl. Acad. Sci. U.S.A.* **103**(20), 7660-7663 (2006).

127. J. Dai and M. P. Sheetz, "Cell membrane mechanics," *Methods. Cell Biol.* **55**, 157-171 (1998).

128. A. Diz-Muñoz, D. A. Fletcher and O. D. Weiner, "Use the force: Membrane tension as an organizer of cell shape and motility," *Trends Cell Biol.* **23**(2), 47-53 (2013).

129. H. Huang, R. D. Kamm and R. T. Lee, "Cell mechanics and mechanotransduction: Pathways, probes, and physiology," *American journal of physiology. Cell physiology* **287**(1), C1-11 (2004).

130. D. W. Schmidtke and S. L. Diamond, "Direct observation of membrane tethers formed during neutrophil attachment to platelets or p-selectin under physiological flow," *J. Cell Biol.* **149**(3), 719-730 (2000).

131. V. Ramachandran, M. Williams, T. Yago, D. W. Schmidtke and R. P. McEver, "Dynamic alterations of membrane tethers stabilize leukocyte rolling on p-selectin," *Proc. Natl. Acad. Sci. U.S.A.* **101**(37), 13519-13524 (2004).

132. H. H. Gerdes, N. V. Bukoreshtliev and J. F. Barroso, "Tunneling nanotubes: A new route for the exchange of components between animal cells," *FEBS Lett.* **581**(11), 2194-2201 (2007).

133. B. Önfelt, S. Nedvetzki, K. Yanagi and D. M. Davis, "Cutting edge: Membrane nanotubes connect immune cells," *J. Immunol.* **173**(3), 1511-1513 (2004).

134. S. Sowinski, C. Jolly, O. Berninghausen, M. A. Purbhoo, A. Chauveau, K. Kohler, S. Oddos, P. Eissmann, F. M. Brodsky, C. Hopkins, B. Onfelt, Q. Sattentau and D. M. Davis, "Membrane nanotubes physically connect t cells over long distances presenting a novel route for hiv-1 transmission," *Nat. Cell Biol.* **10**(2), 211-219 (2008).

135. D. M. Davis and S. Sowinski, "Membrane nanotubes: Dynamic long-distance connections between animal cells," *Nature Reviews Molecular Cell Biology* **9**(6), 431-436 (2008).

136. D. Raucher and M. P. Sheetz, "Membrane expansion increases endocytosis rate during mitosis," *J. Cell Biol.* **144**(3), 497-506 (1999).

137. Z. Li, B. Anvari, M. Takashima, P. Brecht, J. H. Torres and W. E. Brownell, "Membrane tether formation from outer hair cells with optical tweezers," *Biophys. J.* **82**(3), 1386-1395 (2002).

138. A. Datar, T. Bornschlogl, P. Bassereau, J. Prost and P. A. Pullarkat, "Dynamics of membrane tethers reveal novel aspects of cytoskeleton-membrane interactions in axons," *Biophys. J.* **108**(3), 489-497 (2015).

139. J. Dai and M. P. Sheetz, "Mechanical properties of neuronal growth cone membranes studied by tether formation with laser optical tweezers," *Biophys. J.* **68**(3), 988-996 (1995).

140. D. V. Zhelev, D. Needham and R. M. Hochmuth, "A novel micropipet method for measuring the bending modulus of vesicle membranes," *Biophys. J.* **67**(2), 720-727 (1994).

141. H. Zhang and K.-K. Liu, "Optical tweezers for single cells," *J. R. Soc. Interface* **5**(24), 671-690 (2008).

142. H. T. McMahon and J. L. Gallop, "Membrane curvature and mechanisms of dynamic cell membrane remodelling," *Nature* **438**(7068), 590-596 (2005).

143. W. M. Morton, K. R. Ayscough and P. J. McLaughlin, "Latrunculin alters the actin-monomer subunit interface to prevent polymerization," *Nature Cell Biology* **2**(6), 376-378 (2000).

144. F. M. Hochmuth, J. Y. Shao, J. Dai and M. P. Sheetz, "Deformation and flow of membrane into tethers extracted from neuronal growth cones," *Biophys. J.* **70**(1), 358-369 (1996).

145. P. G. Dommersnes, O. Orwar, F. Brochard-Wyart and J. F. Joanny, "Marangoni transport in lipid nanotubes," *Europhys. Lett.* **70**(2), 271 (2005).

146. D. Raucher and M. P. Sheetz, "Characteristics of a membrane reservoir buffering membrane tension," *Biophys. J.* **77**(4), 1992-2002 (1999).

147. N. C. Gauthier, T. A. Masters and M. P. Sheetz, "Mechanical feedback between membrane tension and dynamics," *Trends Cell Biol.* **22**(10), 527-535 (2012).

148. B. Farrell, F. Qian, A. Kolomeisky, B. Anvari and W. E. Brownell, "Measuring forces at the leading edge: A force assay for cell motility," *Integr. Biol.* **5**(1), 204-214 (2013).

149. X. Lei, M. B. Lawrence and C. Dong, "Influence of cell deformation on leukocyte rolling adhesion in shear flow," *J. Biomech. Eng.* **121**(6), 636-643 (1999).

Appendices

Appendix A

The stiffness of the optical tweezers (OTs) used in chapter 2 was calibrated against calculated viscous-drag forces applied on an optically-trapped particle by moving the trapping medium against the particle. The trapped particle was imaged onto a quadrant photodetector (QPD) (Fig. 2.1), and its displacements were tracked using the displacement-calibrated differential voltage readouts of the QPD at 10 KHz. Position standard deviation of a stationary 4.2 μm diameter microsphere was < 10 nm as tracked using the QPD (Fig A.1).

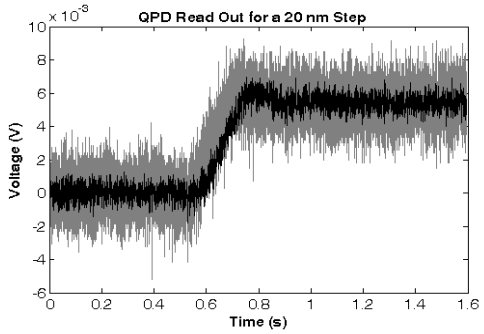

Fig. A.1 QPD voltage readout in response to a 20 nm PZT-controlled displacement of a 4.2 μm diameter microsphere through the focal spot of the laser beam, providing a signal-to-the-noise ratio of >2.

The viscous-drag force applied to the trapped microsphere was calculated as:

$$F_{drag} = \frac{6\pi\eta v r}{1-\frac{9}{16}(\frac{r}{h})+\frac{1}{8}(\frac{r}{h})^3-\frac{45}{256}(\frac{r}{h})^4-\frac{1}{16}(\frac{r}{h})^5} \quad (A.1)$$

where η is the dynamic viscosity of DMEM (1.41 centipoise at 37 °C), v is the fluid velocity induced by the PTZ-controlled displacement of the trapping chamber, r is the radius of the microsphere (2.1 μm), and h is the height of the microsphere from the

bottom of the trapping chamber (12 μm). Particle displacements from the center of the optical trap were tracked using the QPD, and plotted against the viscous-drag forces to calculate the OTs' Hookean stiffness (Fig. A.2).

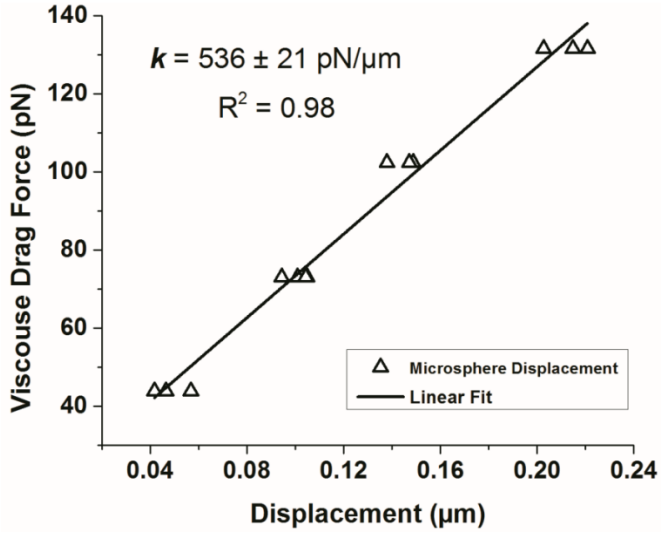

Fig. A.2 Stiffness calibration of the OTs. The Hookean stiffness (k) of the OTs is calculated as the slope of the linear fit to the displacement-force graph ($F=kx$).

Appendix B

Movie captions:

Movie 1 Dynamic quantitative measurement of membrane nanotube structure and reaction force. QPM was performed at 3 fps. The playback is slowed to 2 fps for enhanced viewing. The arrow represents the magnitude and direction of tether reaction force. Color bar is in radians. Scale bar = 10 μm.

Movie 2 Dynamic quantitative measurement of structure and reaction force of a membrane tether formed from a HEK293 cell with intact cytoskeleton. QPI was performed at 4.3 fps. The arrow represents the magnitude of tether reaction force parallel to its axis. Color bar is in nanometers. Scale bar = 4 μm.

Movie 3 Dynamic quantitative measurement of structure and reaction force of a membrane tether formed from a HEK293 cell with disrupted cytoskeleton. QPI was performed at 4.3 fps. The arrow represents the magnitude of tether reaction force parallel to its axis. Color bar is in nanometers. Scale bar = 4 μm.

Appendix C

MATLAB code used in chapter 3 for finding the $M_{1\text{-}4}$ states from the stack of intensity maps recorded at 36 fps.

```
% Disclaimer: This version of the code
%    uses "feature_vec7.m" courtsey of MATLABacademy (opensource)
%    uses "unwrap2.m" courtsey of Carey Smith (opensource)
% end;
%% Loading image for area selection; run only once
clc;
prompt='Select the IMAGE (.TIF) File:  ';
fname=uigetfile('*.tif',prompt);
info = imfinfo(fname);
figure(666)
imagesc(im2double(imread(fname,52)));
[xx,yy]=ginput(2);
xx1=floor(xx(1,1)); xx2=floor(xx(2,1));
yy1=floor(yy(1,1)); yy2=floor(yy(2,1));
close(gcf);
I_back=0;

%% in case images are not already loaded. But the code is based on
saved files
mImage=info(1).Width;
nImage=info(1).Height;
NumberImages=length(info);
bnr=zeros(NumberImages,nImage,mImage,'uint16');

TifLink = Tiff(fname, 'r');
tstart=tic;
fori=1:NumberImages
TifLink.setDirectory(i);
bnr(i,:,:)=TifLink.read();
end
TifLink.close();
tlapsed=toc(tstart)

tstart=tic;
curr=im2double(bnr);
tlapsed=toc(tstart)


%% The CoDE!
%% initializations.run only once

blck=420; %make divisable by 6
full=[30]; %the initializing B
fuA=[]; %this holds A frame positions
fuB=[]; %this holds B frame positions
fuC=[]; %this holds C frame positions
```

```
fuD=[]; %this holds D frame positions
fusuj=[]; %this holds frames suggested by each estimator at each step

% last known good locations fro within the loop
LNGB=0; LNGC=0; LUA=0; LUD=0;

%one time passes for bad data (instead of changing the threshold)
otpB=0; otpC=0;

clear uphi;cleartstmp; clear filler; clear fillerb; clear fillertA;
clear fillertB; clear fillertC; clear fillertD; clear filler; clear
efeA; clear defeB; clear defeC; clear defeD; clear M; clear Mb;
flagL=0;flagS=0;lfL=[];lfS=[];lfM=[];mk1=[];mk2=[]; clear indx;

%[double] images are previously loaded and stored in files. we clear
the memory, and bring in the data in at smaller blocks
%The smaller the block, the more frequent hard needs to be accessed. so
%optimize!
file1=matfile('18CURRCR.mat'); % The image file
file2=matfile('18CURRCRBINRo.mat'); % The mask file based on the image

%% Frame info finder (for resetting bad frames and resuming search)
frm=input('\n Enter the Bad frame''s number: ');
frm=frm-1;
if (frm/2-floor(frm/2))~=0
fprintf('\n Broken at B \n Frame was made of: C= %u, A= %u, D= %u, B=
%u \n', fuC(floor((frm-1)/2)), fuA(frm-1+1), fuD(frm-1+1),
fuB(floor((frm)/2)+1));
fprintf(' LNGC(s) = %u , %u, LNGB = %u \n set pfn = %u , fsho=sh = %u ,
lup= %u \n\n', fuC(floor((frm-1)/2)-1),fuC(floor((frm-1)/2)),
fuB(floor((frm-1)/2)), frm-2, fuD(frm-1+1), floor(fuD(frm-
1+1)/blck)+1);
ansr=input('\n reset values? (0 / 1)  ');
ifansr==true
lup=floor(fuD(frm+1)/blck)+1;
pfn=frm-2;
sh=fuD(frm-1+1);
fsho=sh;
full=full(1:find(full==fuC(floor((frm-1)/2))));
fuA=fuA(1:frm-1);
fuB=fuB(1:floor((frm-1)/2));
fuC=fuC(1:floor((frm-1)/2));
fuD=fuD(1:frm-1);
end;
end;
if (frm/2-floor(frm/2))==0
fprintf('\n Broken at C \n Frame was made of: B= %u, D= %u, A= %u, C=
%u \n', fuB(floor((frm-1)/2)+1), fuD(frm-1+1), fuA(frm-1+1),
fuC(floor((frm-1)/2)+1));
fprintf(' LNGC = %u, LNGB = %u \n set pfn = %u , fsho=sh = %u , lup= %u
\n\n', fuC(floor((frm-1)/2)), fuB(floor((frm-1)/2)+1), frm-3, fuD(frm-
2+1), floor(fuD(frm+1)/blck)+1);
ansr=input('\n reset values? (0 / 1)  ');
```

```
ifansr==true
lup=floor(fuD(frm+1)/blck)+1;
pfn=frm-3;
sh=fuD(frm-2+1);
fsho=sh;
full=full(1:find(full==fuC(floor((frm-1)/2))));
fuB=fuB(1:floor((frm)/2));
fuD=fuD(1:frm-2+1);
fuA=fuA(1:frm-2+1);
fuC=fuC(1:floor((frm-1)/2));
end;
end;

%% the calculating body
rfac=6.5; %intensity adjustment for phase calculation
lup=1; %first time. the big loop counter
pfn=0; %first time. This is your result counter
sh=69; %begining point, first time, the "D" right before the first 2-4-
1-3-1-4-2
fsho=sh; %Checks: if equal, goes through initialization

% Quality of every estimator for detecting each of the shifts.
% Adjust for the current set as you go, based on the suggestions log
(fusuj)
Zr1=[NaNNaNNaNNaNNaN 1 NaN];
Zr2=[0.3 NaNNaNNaNNaN 0.7 1 NaN];
Zr3=[0.5 0.3 0.7 NaNNaNNaN 1 NaN];
Zr4=[NaN 0.7 0.5 0.7 0.5 NaN 1 NaN];
Zr5=[NaNNaNNaNNaNNaNNaN 1 NaN];
Zr6=[NaNNaNNaN 1 1 NaN 1 1];

thrsh=1000; % results variation accepted threshold

% Last known good (input) frames of each state. reset before each run
LC=989;
LA=991;
LD=993; %make sure it's comparable to sh; should be the "D" right
before the first 2-4-1-3-1-4-2
LB=996;

%otpB=true;
%otpC=true;

tstart1=tic;% how much data to take in every time to avoid overflowing
the ram and slowing down the code

while lup <= floor(length(info)/blck)+1  %each time reads in a blck
size of frame and analyzes them

    tstart2=tic;

clear curr;
```

```
clear bnr;

    curr=file1.curr(min((lup-
1)*blck+1,sh):min((lup*blck)+30,length(info)),:,:);
    bnr=file2.curr(min((lup-
1)*blck+1,sh):min((lup*blck)+30,length(info)),:,:);

if fsho==sh %initialization values on the first run

full=[full ; LA; LD];
fuA=[fuA ; LA];
fuD=[fuD ; LD];

            LNGB=LB;
            LNGC=LC;

fillertA(:,:)=file1.curr(LA,:,:);
fillertbA(:,:)=file2.curr(LA,:,:);
fillertB(:,:)=file1.curr(LB,:,:);
fillertbB(:,:)=file2.curr(LB,:,:);
fillertC(:,:)=file1.curr(LC,:,:);
fillertbC(:,:)=file2.curr(LC,:,:);
fillertD(:,:)=file1.curr(LD,:,:);
fillertbD(:,:)=file2.curr(LD,:,:);

            MA=feature_vec7(fillertA);
            MB=feature_vec7(fillertB);
            MC=feature_vec7(fillertC);
            MD=feature_vec7(fillertD);

MAb=feature_vec7(fillertbA);
MBb=feature_vec7(fillertbB);
MCb=feature_vec7(fillertbC);
MDb=feature_vec7(fillertbD);
            %% Resolve the initial one here and store
            A=fillertA;
            B=fillertB;
            C=fillertC;
            D=fillertD;

Gs=(D-B); Gc=A-C; del_phi=atan2(Gs,Gc);
%beta
            L=(A-C+D-B)./(sin(del_phi)+cos(del_phi))/4; %E0*E1
            g1=(A+C)/2; %E0^2+E1^2=s
            g2=L.*L; %E0^2*E1^2=p
x1=g1/2-sqrt(g1.*g1-4*g2)/2; x2=g1/2+sqrt(g1.*g1-4*g2)/2; %solutions
            beta1=sqrt(x1./x2); beta2=1./beta1;
%get constant from  average over pixels
cL=L(yy1:yy2,xx1:xx2); cbeta1=beta1(yy1:yy2,xx1:xx2);
            L1=real(mean2(cbeta1))/mean2(cL);
            LL=L1*L;
```

```
beta=LL*rfac; %real beta, ADJUSTED BASED ON CALIBRATION (BECAUSE OF
CHANGES IN INTENSITY)
phi=atan2(beta.*sin(del_phi),1+beta.*cos(del_phi));
pfn=pfn+1;
            REZ=unwrap2(phi);
uphi(:,:,pfn)=REZ;

end;

while sh<(min((lup*blck),length(info)))

shs=sh; %non-creeping counter for the loop

% 4-2

          MDUM=MB;
MDUMb=MBb;
fillerR=fillertB;
fillerRb=fillertbB;
for c=1:4
filler(:,:)=curr(sh+c-min((lup-1)*blck,sh-1),:,:);
fillerb(:,:)=bnr(sh+c-min((lup-1)*blck,sh-1),:,:);
          M(c,:)=[abs(feature_vec7(filler)-MDUM);
abs(sum(sum(abs(filler-fillerR))));abs(sum(sum((filler-fillerR))))];
          Mb(c,:)=[abs(feature_vec7(fillerb)-MDUMb);
abs(sum(sum(abs(fillerb-fillerRb))));abs(sum(sum((fillerb-
fillerRb))))];
end;

        [dum,ind3]=min(M);
        [dum,ind2]=min(Mb);

        M1=(max(M)-min(M))./mean(M).*Zr1;
        M2=(max(Mb)-min(Mb))./mean(Mb).*Zr1;

        [dum,vs1]=max(M1);mk1=[mk1;ind3(vs1)];
        [dum,vs2]=max(M2);mk2=[mk2;ind2(vs2)];
        ind1=[vs1+2 vs2+10 ind3+sh ind2+sh];
        M1(vs1)=NaN;[dum,vs1]=max(M1);mk1=[mk1;ind3(vs1)];
fusuj=[fusuj; ind1];
        M2(vs2)=NaN;[dum,vs2]=max(M2);mk2=[mk2;ind2(vs2)];

indx=intersect(mk1,mk2);
if length(indx) ~= 1
lfM=[lfM;sh];indl=mk2(1); %priority between full image(1) and binary(2)
elseindl=indx;
end;
sh=sh+indl;
          mk1=[];mk2=[]; clear indx;

full=[full ; sh];
fuB=[fuB ; sh];
```

```
fillertB(:,:)=curr(sh-min((lup-1)*blck,shs-1),:,:);
fillertbB(:,:)=bnr(sh-min((lup-1)*blck,shs-1),:,:);


        %% RESOLVE ONE HERE AND COMPARE (first one)

        A=fillertA;
        B=fillertB;
        C=fillertC;
        D=fillertD;

Gs=(D-B); Gc=A-C; del_phi=atan2(Gs,Gc);
%beta
        L=(A-C+D-B)./(sin(del_phi)+cos(del_phi))/4; %E0*E1
        g1=(A+C)/2; %E0^2+E1^2=s
        g2=L.*L; %E0^2*E1^2=p
x1=g1/2-sqrt(g1.*g1-4*g2)/2; x2=g1/2+sqrt(g1.*g1-4*g2)/2; %solutions
        beta1=sqrt(x1./x2); beta2=1./beta1;
%get constant from  average over pixels
cL=L(yy1:yy2,xx1:xx2); cbeta1=beta1(yy1:yy2,xx1:xx2);
        L1=real(mean2(cbeta1))/mean2(cL);
        LL=L1*L;
beta=LL*rfac; %real beta, ADJUSTED BASED ON CALIBRATION (BECAUSE OF
CHANGES IN INTENSITY)
phi=atan2(beta.*sin(del_phi),1+beta.*cos(del_phi));
pfn=pfn+1;
uphi(:,:,pfn)=unwrap2(phi);
tstmp(pfn)=abs((full(end)-full(end-3)))*0.028;


ifotpB ~= true
if abs(sum(abs(sum((uphi(:,:,pfn)-REZ))))) >thrsh
abs(sum(abs(sum((uphi(:,:,pfn)-REZ)))))
sh=fuD(pfn-1);%fuA and fuD are 1 element longer
fsho=sh;
full=full(1:find(full==fuC(floor((pfn-1)/2))));
                LUA=fuA(pfn-1);
                LUD=fuD(pfn-1);
fuA=fuA(1:pfn-2);%fuA and fuD are 1 element longer
fuB=fuB(1:floor((pfn-1)/2));
fuC=fuC(1:floor((pfn-1)/2));
fuD=fuD(1:pfn-2);%fuA and fuD are 1 element longer

for k=pfn-2:pfn
figure(k)
surf(-1.88*uphi(:,:,k),'FaceColor','interp', 'EdgeColor','none',
'FaceLighting','flat')
view(141,80), camlightleft , axis off
title(['t= ' num2str(sum(tstmp(1:k))) '
s'],'fontweight','bold','FontSize',16)
xlabel('X Pixels'), ylabel('Y Pixels'), zlabel('Phase in mrad')
caxismanual
```

```
caxis([-1 1.5]);
colorbar;
end;
pfn=pfn-2;
loadhandel
sound(y,Fs)
error(fprintf('\n Broken at B \n LNGB = %u, LGNC = %u ,(A%u)(D%u)  (bad
pfn: %u)\n', LNGB,  LNGC, LUA, LUD, pfn+2));
end;
end;
pfn
tlapsedF=toc(tstart1)
                REZ=uphi(:,:,pfn);
                LNGB=sh;
otpB=false;
%otpB=true;
%%

       MB=feature_vec7(fillertB);
MBb=feature_vec7(fillertbB);


% 2-4
          MDUM=MD;
MDUMb=MDb;
fillerR=fillertD;
fillerRb=fillertbD;
for c=1:4
filler(:,:)=curr(sh+c-min((lup-1)*blck,sh-1),:,:);
fillerb(:,:)=bnr(sh+c-min((lup-1)*blck,sh-1),:,:);
          M(c,:)=[abs(feature_vec7(filler)-MDUM);
abs(sum(sum(abs(filler-fillerR))));abs(sum(sum((filler-fillerR))))];
          Mb(c,:)=[abs(feature_vec7(fillerb)-MDUMb);
abs(sum(sum(abs(fillerb-fillerRb))));abs(sum(sum((fillerb-
fillerRb))))];

end;


         [dum,ind2]=min(Mb);
         [dum,ind3]=min(M);
         M1=(max(M)-min(M))./mean(M).*Zr2;
         M2=(max(Mb)-min(Mb))./mean(Mb).*Zr2;

         [dum,vs1]=max(M1);mk1=[mk1;ind3(vs1)];
         [dum,vs2]=max(M2);mk2=[mk2;ind2(vs2)];
         ind1=[vs1+2 vs2+10 ind3+sh ind2+sh];
         M1(vs1)=NaN;[dum,vs1]=max(M1);mk1=[mk1;ind3(vs1)];
fusuj=[fusuj; ind1];
         M2(vs2)=NaN;[dum,vs2]=max(M2);mk2=[mk2;ind2(vs2)];

indx=intersect(mk1,mk2);
```

```
if length(indx) ~= 1
lfM=[lfM;sh];indl=mk2(1); %priority between full image(1) and binary(2)
elseindl=indx;
end;
sh=sh+indl;
           mk1=[];mk2=[]; clear indx;
full=[full ; sh];
fuD=[fuD ; sh];

fillertD(:,:)=curr(sh-min((lup-1)*blck,shs-1),:,:);
fillertbD(:,:)=bnr(sh-min((lup-1)*blck,shs-1),:,:);
        MD=feature_vec7(fillertD);
MDb=feature_vec7(fillertbD);

% 4-1
        MDUM=MA;
MDUMb=MAb;
fillerR=fillertA;
fillerRb=fillertbA;
for c=1:4
filler(:,:)=curr(sh+c-min((lup-1)*blck,sh-1),:,:);
fillerb(:,:)=bnr(sh+c-min((lup-1)*blck,sh-1),:,:);
          M(c,:)=[abs(feature_vec7(filler)-MDUM);
abs(sum(sum(abs(filler-fillerR))));abs(sum(sum((filler-fillerR))))];
          Mb(c,:)=[abs(feature_vec7(fillerb)-MDUMb);
abs(sum(sum(abs(fillerb-fillerRb))));abs(sum(sum((fillerb-
fillerRb))))];

end;


        [dum,ind2]=min(Mb);
        [dum,ind3]=min(M);

        M1=(max(M)-min(M))./mean(M).*Zr3;
        M2=(max(Mb)-min(Mb))./mean(Mb).*Zr3;

        [dum,vs1]=max(M1);mk1=[mk1;ind3(vs1)];
        [dum,vs2]=max(M2);mk2=[mk2;ind2(vs2)];
        ind1=[vs1+2 vs2+10 ind3+sh ind2+sh];
        M1(vs1)=NaN;[dum,vs1]=max(M1);mk1=[mk1;ind3(vs1)];
fusuj=[fusuj; ind1];
        M2(vs2)=NaN;[dum,vs2]=max(M2);mk2=[mk2;ind2(vs2)];

indx=intersect(mk1,mk2);
if length(indx) ~= 1
lfM=[lfM;sh];indl=mk2(1); %priority between full image(1) and binary(2)
elseindl=indx;
end;
sh=sh+indl;
           mk1=[];mk2=[]; clear indx;
full=[full ; sh];
```

```
fuA=[fuA ; sh];


fillertA(:,:)=curr(sh-min((lup-1)*blck,shs-1),:,:);
fillertbA(:,:)=bnr(sh-min((lup-1)*blck,shs-1),:,:);
        MA=feature_vec7(fillertA);
MAb=feature_vec7(fillertbA);

% 1-3
        MDUM=MC;
MDUMb=MCb;
fillerR=fillertC;
fillerRb=fillertbC;
for c=1:4
filler(:,:)=curr(sh+c-min((lup-1)*blck,sh-1),:,:);
fillerb(:,:)=bnr(sh+c-min((lup-1)*blck,sh-1),:,:);
          M(c,:)=[abs(feature_vec7(filler)-MDUM);
abs(sum(sum(abs(filler-fillerR))));abs(sum(sum((filler-fillerR))))];
          Mb(c,:)=[abs(feature_vec7(fillerb)-MDUMb);
abs(sum(sum(abs(fillerb-fillerRb))));abs(sum(sum((fillerb-
fillerRb))))];

end;


         [dum,ind2]=min(Mb);
         [dum,ind3]=min(M);

         M1=(max(M)-min(M))./mean(M).*Zr4;
         M2=(max(Mb)-min(Mb))./mean(Mb).*Zr4;

         [dum,vs1]=max(M1);mk1=[mk1;ind3(vs1)];
         [dum,vs2]=max(M2);mk2=[mk2;ind2(vs2)];
         ind1=[vs1+2 vs2+10 ind3+sh ind2+sh];
         M1(vs1)=NaN;[dum,vs1]=max(M1);mk1=[mk1;ind3(vs1)];
fusuj=[fusuj; ind1];
         M2(vs2)=NaN;[dum,vs2]=max(M2);mk2=[mk2;ind2(vs2)];

indx=intersect(mk1,mk2);
if length(indx) ~= 1
lfM=[lfM;sh];indl=mk2(1); %priority between full image(1) and binary(2)
elseindl=indx;
end;
sh=sh+indl;
           mk1=[];mk2=[]; clear indx;
full=[full ; sh];
fuC=[fuC ; sh];

fillertC(:,:)=curr(sh-min((lup-1)*blck,shs-1),:,:);
fillertbC(:,:)=bnr(sh-min((lup-1)*blck,shs-1),:,:);
```

```
  %% RESOLVE ONE HERE AND COMPARE (second one)
        A=fillertA;
        B=fillertB;
        C=fillertC;
        D=fillertD;
Gs=(D-B); Gc=A-C; del_phi=atan2(Gs,Gc);
%beta
        L=(A-C+D-B)./(sin(del_phi)+cos(del_phi))/4; %E0*E1
        g1=(A+C)/2; %E0^2+E1^2=s
        g2=L.*L; %E0^2*E1^2=p
x1=g1/2-sqrt(g1.*g1-4*g2)/2; x2=g1/2+sqrt(g1.*g1-4*g2)/2; %solutions
        beta1=sqrt(x1./x2); beta2=1./beta1;
%get constant from  average over pixels
cL=L(yy1:yy2,xx1:xx2); cbeta1=beta1(yy1:yy2,xx1:xx2);
        L1=real(mean2(cbeta1))/mean2(cL);
        LL=L1*L;
beta=LL*rfac; %real beta, ADJUSTED BASED ON CALIBRATION (BECAUSE OF
CHANGES IN INTENSITY)
phi=atan2(beta.*sin(del_phi),1+beta.*cos(del_phi));
pfn=pfn+1;
uphi(:,:,pfn)=unwrap2(phi);
tstmp(pfn)=abs((full(end)-full(end-3)))*0.028;

ifotpC ~= true
if abs(sum(abs(sum((uphi(:,:,pfn)-REZ)))))>thrsh
abs(sum(abs(sum((uphi(:,:,pfn)-REZ)))))
sh=fuD(pfn-2); %fuA and fuD are 1 element longer
fsho=sh;
                LUA=fuA(pfn-2);
                LUD=fuD(pfn-2);
full=full(1:find(full==fuC(floor(pfn/2)-1)));
fuB=fuB(1:floor(pfn/2)-1);
fuD=fuD(1:pfn-3);%fuA and fuD are 1 element longer
fuA=fuA(1:pfn-3);%fuA and fuD are 1 element longer
fuC=fuC(1:floor(pfn/2)-1);
for k=pfn-2:pfn
figure(k)
surf(-1.88*uphi(:,:,k),'FaceColor','interp', 'EdgeColor','none',
'FaceLighting','flat')
view(141,80), camlightleft , axis off
title(['t= ' num2str(sum(tstmp(1:k))) '
s'],'fontweight','bold','FontSize',16)
xlabel('X Pixels'), ylabel('Y Pixels'), zlabel('Phase in mrad')
caxismanual
caxis([-1 1.5]);
colorbar;
end;
pfn=pfn-3;
loadhandel
sound(y,Fs)
error(fprintf('\n Broken at C \n LGNC = %u (A%u)(D%u), LNGB = %u   (bad
pfn: %u)\n',LNGC,LUA,LUD, LNGB,  pfn+3));
end;
```

```
end;
otpC=false;
%otpC=true;
pfn
tlapsedF=toc(tstart1)
        REZ=uphi(:,:,pfn);
        LNGC=sh;
%%
        MC=feature_vec7(fillertC);
MCb=feature_vec7(fillertbC);

% 3-1
          MDUM=MA;
MDUMb=MAb;
fillerR=fillertA;
fillerRb=fillertbA;
for c=1:4
filler(:,:)=curr(sh+c-min((lup-1)*blck,sh-1),:,:);
fillerb(:,:)=bnr(sh+c-min((lup-1)*blck,sh-1),:,:);
          M(c,:)=[abs(feature_vec7(filler)-MDUM);
abs(sum(sum(abs(filler-fillerR))));abs(sum(sum((filler-fillerR))))];
          Mb(c,:)=[abs(feature_vec7(fillerb)-MDUMb);
abs(sum(sum(abs(fillerb-fillerRb))));abs(sum(sum((fillerb-
fillerRb))))];
end;
        [dum,ind2]=min(Mb);
        [dum,ind3]=min(M);
        M1=(max(M)-min(M))./mean(M).*Zr5;
        M2=(max(Mb)-min(Mb))./mean(Mb).*Zr5;
        [dum,vs1]=max(M1);mk1=[mk1;ind3(vs1)];
        [dum,vs2]=max(M2);mk2=[mk2;ind2(vs2)];
        ind1=[vs1+2 vs2+10 ind3+sh ind2+sh];
        M1(vs1)=NaN;[dum,vs1]=max(M1);mk1=[mk1;ind3(vs1)];
fusuj=[fusuj; ind1];
        M2(vs2)=NaN;[dum,vs2]=max(M2);mk2=[mk2;ind2(vs2)];
indx=intersect(mk1,mk2);
if length(indx) ~= 1
lfM=[lfM;sh];indl=mk1(1); %priority between full image(lm1) and
binary(lm2)
elseindl=indx;
end;
sh=sh+indl;
          mk1=[];mk2=[]; clear indx;
full=[full ; sh];
fuA=[fuA ; sh];
fillertA(:,:)=curr(sh-min((lup-1)*blck,shs-1),:,:);
fillertbA(:,:)=bnr(sh-min((lup-1)*blck,shs-1),:,:);
        MA=feature_vec7(fillertA);
MAb=feature_vec7(fillertbA);

% 1-4
          MDUM=MD;
MDUMb=MDb;
```

```
fillerR=fillertD;
fillerRb=fillertbD;
for c=1:4
filler(:,:)=curr(sh+c-min((lup-1)*blck,sh-1),:,:);
fillerb(:,:)=bnr(sh+c-min((lup-1)*blck,sh-1),:,:);
          M(c,:)=[abs(feature_vec7(filler)-MDUM);
abs(sum(sum(abs(filler-fillerR))));abs(sum(sum((filler-fillerR))))];
          Mb(c,:)=[abs(feature_vec7(fillerb)-MDUMb);
abs(sum(sum(abs(fillerb-fillerRb))));abs(sum(sum((fillerb-
fillerRb))))];

end;
         [dum,ind2]=min(Mb);
         [dum,ind3]=min(M);
         M1=(max(M)-min(M))./mean(M).*Zr6;
         M2=(max(Mb)-min(Mb))./mean(Mb).*Zr6;
         [dum,vs1]=max(M1);mk1=[mk1;ind3(vs1)];
         [dum,vs2]=max(M2);mk2=[mk2;ind2(vs2)];
         ind1=[vs1+2 vs2+10 ind3+sh ind2+sh];
         M1(vs1)=NaN;[dum,vs1]=max(M1);mk1=[mk1;ind3(vs1)];
fusuj=[fusuj; ind1];
         M2(vs2)=NaN;[dum,vs2]=max(M2);mk2=[mk2;ind2(vs2)];
indx=intersect(mk1,mk2);
if length(indx) ~= 1
lfM=[lfM;sh];indl=mk2(1); %priority between full image(lm1) and
binary(lm2)
elseindl=indx;
end;
sh=sh+indl;
           mk1=[];mk2=[]; clear indx;
full=[full ; sh];
fuD=[fuD ; sh];
fillertD(:,:)=curr(sh-min((lup-1)*blck,shs-1),:,:);
fillertbD(:,:)=bnr(sh-min((lup-1)*blck,shs-1),:,:);
         MD=feature_vec7(fillertD);
MDb=feature_vec7(fillertbD);

% Flags for short and long frames
if (sh-shs)>22
flagL=flagL+1;
lfL=[lfL ; sh];
end;
if (sh-shs)<16
flagS=flagS+1;
lfS=[lfS ; sh];
end;

end;
          tlapsed2=toc(tstart2)
          tlapsed1=toc(tstart1)/60
lup=lup+1;
end;
```